Please cite the Published Version

Lin, M, Nemcova, A, Voevodin, AA, Korenyi-Both, A, Liskiewicz, TW, Laugel, N, Matthews, A and Yerokhin, A (2021) Surface characteristics underpinning fretting wear performance of heavily loaded duplex chameleon/PEO coatings on Al. Tribology International, 154. 106723 ISSN 0301-679X

DOI: https://doi.org/10.1016/j.triboint.2020.106723

Publisher: Elsevier

Version: Accepted Version

Surface characteristics underpinning fretting wear performance of heavily loaded duplex chameleon/PEO coatings on Al

Mengyu Lin[1], Aneta Nemcova[1], Andrey A. Voevodin[2], Andras Korenyi-Both[3], Tomasz W. Liskiewicz[4], Nicolas Laugel[1], Allan Matthews[1], and Aleksey Yerokhin[1]*

[1] Department of Materials, the University of Manchester, Oxford Road, Manchester, M13 9PL, UK
[2] Department of Materials Science and Engineering, University of North Texas, Denton, TX 76203, USA
[3] Dept. of Metallurgical & Materials Engineering, Colorado School of Mines, Golden, CO 80401, USA
[4] Faculty of Science and Engineering, Manchester Metropolitan University, John Dalton Building, Chester Street, Manchester, M15 6BH, UK

Abstract

Duplex coatings comprising MoS_2/Sb_2O_3/graphite layer burnished on top of plasma electrolytically oxidised AA6082 alloy enhanced fretting wear resistance against alumina and steel whilst reducing friction from ~0.6…0.9 to ~0.08…0.1 in dry nitrogen and humid air. Transitions to stick-slip (~3 μm), partial slip (5-10 μm) and gross slip (>10 μm) showed an order of magnitude improvements over single-layer PEO coatings. In the latter mode, high initial contact pressures (~1.1 GPa) with steel counterpart under oxidising atmosphere increased friction due to generation of Fe/Al/Cr oxides/hydroxides in the contact region, leading micro-cracking in PEO coating followed by fatigue damage of aluminium substrate. Reducing contact pressure <1 GPa, retained topcoat lubricating behaviour, high wear resistance and eliminated fatigue damage after 10^4 cycles.

Keywords:

Fretting wear; Solid lubrication; Duplex coating; Al alloy

* Corresponding Author. E-mail address: Aleksey.Yerokhin@manchester.ac.uk

1. Introduction

Aluminium and its alloys have been widely used in the aerospace and automobile industries due to outstanding properties, such as a high strength-to-weight ratio, an excellent thermal conductivity and a relatively low density [1, 2]. Despite these advantages, low hardness and poor wear resistance have severely restricted the industrial applications of aluminium alloys in mechanical engineering applications where surface load-bearing capacities are crucial. Hard ceramic coatings may effectively increase the wear resistance of aluminium alloys. Therefore, various surface treatments such as thermal spraying [3], physical and chemical vapour deposition [4, 5] have been considered to enhance their surface mechanical properties. However, challenges of adhesion, high processing temperatures up to 500-1000 °C, and low thickness (in some cases) reduce their applicability for wear protection of aluminium alloy substrates [6, 7]. A viable alternative to these techniques is Plasma Electrolytic Oxidation (PEO), which has now become a well-established technology to produce coatings with relatively high hardness and thickness [6-10], good corrosion resistance [8] and excellent adhesion to the Al substrate [9]. During PEO treatments that are carried out at near to ambient bulk substrate temperatures, aluminium alloy surfaces undergo a series of localised plasma-assisted electrochemical conversions resulting in formation and growth of oxide ceramic layers with complex composition based on crystalline α and γ Al_2O_3 phases. Since the hard α-alumina phase usually appears once the oxide layer has grown to a certain thickness and becomes relatively dense, it is generally considered that only relatively thick (50 to 150 μm) PEO coatings would provide adequate hardness and load support to enhance the abrasion resistance of aluminium alloys in sliding wear under moderate loads [9, 10]. However, recent advances in PEO technology [11, 12] enable accelerated formation of α-alumina under controlled conditions of pulsed reverse polarisation, where impact of plasma discharge on the coating growth is reduced. Consequently, it becomes possible obtaining thin (20 to 30 μm) yet dense and hard PEO coatings suitable for load-bearing tribological application.

A group of relevant applications, for which the protective capacity of PEO coatings has so far been poorly understood, includes situations where material integrity can be compromised due to fretting. In contrast to sliding, fretting wear normally occurs between two contacting surfaces under small-amplitude vibration causing displacements in the order of 1-10 μm [13, 14]. It is typically encountered at bolts, joints and bearing races in many vital industrial structures, such as the gas turbine engines [15], power plant machineries [16], cables [17] and even some biomedical implants [18]. The oscillatory tangential displacement that occurs during fretting wear degrades the surface quality and leads to the surface material removal as well as fatigue crack nucleation and propagation [14]. Three distinct main fretting regimes have been defined. The stick-slip fretting regime occurs in very low displacement amplitudes (typically below 5 μm) with no visible surface wear damages but accumulation of fatigue due to the repeated elastic stressing; stick-slip sliding occurs in higher amplitudes (around 2-10 μm) with a central no-slip region and a slip-annulus damaged region; gross sliding occurs in the highest amplitudes (above 10-20 μm) with full wear track and extensive plastic shear [19-21]. In the pure stick fretting regime, the fatigue induced cracking may lead to catastrophic failures with little warning by observable wear and this mode is especially dangerous for aluminium alloys which, unlike steels, do not have a fatigue stress limit. In the mixed stick-slip sliding regime, the tangential force increases as adhesive contact regions form, and wear debris is released due to accumulation of both wear damage and development of fatigue micro-cracks [22]. Hard particles originated from either the counterpart material or the outer layer of the coated sample lead to accelerated wear, precipitating catastrophic surface failure [23, 24]. Under gross sliding regime, the extensive plastic shear leads to the contact surface deformation and formation of tribofilms, so that the modified top surface layer is usually described as a tribologically transformed structure (TTS) which is hard but fragile [25]. The TTS layer would gradually disintegrate and release wear debris in the contact areas [25, 26]. Since the occurrence of fretting appears inevitable in most mechanical engineering applications under vibration and cyclic stress, efforts are made to reduce fretting wear and extend the lifetime of engineering structures. Among promising approaches, application of solid lubricants on susceptible contact areas is considered to avoid catastrophic fatigue failure under pure stick and stick-slip contact regimes.

For aerospace applications, where aluminium alloys are widely used, the additional challenging aspect of the fretting wear protection are variable working environments, such as harsh external atmospheres, pressures and temperatures. Liquid lubricants in this context are liable to significant performance degradations. Solid lubricants, in turn, constitute a viable alternative to provide sufficient tribological performance over a wider range of working environments. To overcome the variable and cycled environmental challenges of aerospace applications, adaptable duplex chameleon/PEO coatings were recently introduced [27]. The majority of chameleon materials are composed of transition-metal dichalcogenides and graphite, while some may have inclusions on low shear strength metals and oxide phases [28]. Transition-metal dichalcogenides, for which the most well-known compound is MoS_2, have been proved to provide low friction and great lubrication in vacuum. However, MoS_2 has also been reported to be sensitive to ambient temperature and humidity. It has moreover been found that MoS_2 deteriorates and breaks down under elevated temperatures and is highly susceptible to water adsorption and oxidation during friction [29]. In contrast, graphite has been demonstrated to offer effective lubrication in humid ambient environment while losing its superior properties in dry or vacuum atmosphere. Combining those two solid lubricants provides a beneficial blend of self-lubrication [30, 31], long wear lifetime [31] and high-wear resistance under various environments [28]. Many multiphase chameleon coatings have been investigated and reported. WC/DLC & TiC/DLC & WC/DLC/WS_2 coatings (where DLC signifies hydrogen-free diamond-like carbon) were prepared onto stainless steel substrates and showed low friction both in dry nitrogen, vacuum and humid air environment [31]. Al_2O_3/DLC/Au/MoS_2 coatings were prepared on different substrates using hybrid magnetron sputtering/pulsed laser deposition (MSPLD) and showed low friction both in dry nitrogen and humid air environment [32]. Multi-layered YSZ/Ag/MoS_2 coatings (where YSZ stands for yttria-stabilised zirconia) also maintained low friction for more than 2.5×10^4 cycles, with significant increases in wear lifetimes [33]. SiC/Ag and HfC/Ag films deposited by magnetron sputtering showed good wear resistance and low friction coefficient for over 10^4 cycles [34]. However, some of the chameleon coatings deposited by magnetron sputtering demonstrated a relatively poor adhesion to the substrates [28]. The relatively compact structure of PEO coatings and their excellent adhesion to the aluminium alloy surfaces can greatly enhance the attachment of solid lubricant coatings [9]. In recent years, several solid lubricants have been applied onto PEO-coated alloys [35, 36]. A multi-layered PEO/Ag/MoS_2 coating was deposited on Ti6Al4V, and its tribological properties were evaluated by ball-on-disk tribometry at elevated temperatures [35]. The effective MoS_2 and Ag lubricants resulted in reduction in friction coefficient and high wear resistance both under ambient and moderately elevated (350 °C) temperatures. At the same time, the investigations of PEO combination with chameleon solid lubricants under fretting regimes of aluminium alloys are largely unexplored. We recently reported that such combination can indeed provide a significant reduction in fretting wear of aluminium alloys [27], but the understanding of surface evolution and the adaptation mechanisms of the chameleon/PEO coated aluminium surfaces under different fretting wear conditions is still lacking.

To address this issue, the present study was focused on the evolution of a duplex coating comprising a chameleon (graphite/MoS_2/Sb_2O_3) layer burnished on the top of a PEO layer grown on 6082 series aluminium alloy during fretting tests performed in ambient humid air and dry nitrogen atmosphere against alumina and steel counterparts, at displacement amplitudes (3 μm to 100 μm) corresponding to fretting regimes ranging from stick to gross slip mode.

2. Experimental

2.1 Material and coatings deposition

The plasma electrolytic oxidation (PEO) coating was grown to a thickness of approximately 20 μm on a 6082 series aluminium alloy plate with dimensions of 50 mm by 50 mm by 1.5 mm in the aqueous electrolyte solution containing 1-2 g/l of KOH, 1-2 g/l of Na_2SiO_3 and 2-3 g/l of $Na_4P_2O_7 \cdot 10H_2O$. A pulsed reversed polarisation was applied at 1.7 kHz frequency with positive and negative bias amplitudes of +530 V and -180 V respectively, resulting in an initial RMS current density of 30 A/dm^2. Powders of pure graphite, MoS_2 and Sb_2O_3 were subsequently mixed in a 2:2:1 weight ratio and burnished onto the surface of the PEO coating using a lint free cloth under hand pressure. Further details of the coatings preparation can be found elsewhere [9, 37].

2.2 Fretting wear tests

The duplex chameleon/PEO coatings were tested at room temperature (22 ^{o}C) using a ball-on-plane reciprocal fretting tribometer operating at 3 Hz. Two different counterpart materials were utilised: a 12 mm diameter 440 stainless steel ball (58-60 HRC, E ~ 200 GPa) and a 16 mm diameter alumina ball (HV ≈ 12-15 GPa, E ~ 280 GPa), both with surface roughness Ra ≈ 0.08-0.1 μm. Following our former report [27], a full gross-slip fretting regime of the PEO coating could be induced at >60 μm displacement amplitudes and with a 75 N normal load which provided the initial Hertzian contact pressure of about 1.6 GPa. The fretting wear tests of the duplex coatings in the present work were divided into two parts with different experimental parameters and goals, as explained below.

To identify surface evolution under fretting regimes, in the first group of tests, displacement amplitudes were increased in steps from 3 μm, 5 μm, 10 μm, 20 μm to 100 μm. These tests were conducted in a humid air environment for $1x10^3$ cycles, which was deemed sufficient to pass initial stages where major structural transformations in materials usually take place [38] and reach steady-state fretting regimes. Normal loads of 15 N and 20 N were applied on steel and alumina balls respectively; these provided corresponding estimates of initial contact radii at 86 and 99 μm, resulting in a similar initial contact pressure of ~0.96 GPa. Critical transition between pure stick fretting, partial-slip sliding and gross-slip sliding regimes were observed and the conditions under which they occurred were characterised.

Additionally, a load bearing capacity of the hard PEO layer in the duplex chameleon/PEO coating system was evaluated in the gross slip sliding mode (100 μm displacement amplitude) by increasing the initial contact pressure to about 1.1 GPa when applying a 20 N normal load on the steel ball. In the second group of tests, environmental adaptability of the duplex coatings in humid air and dry nitrogen atmosphere was investigated. The gross slip conditions were maintained for 1×10^4 fretting cycles at initial contact pressures of 973/980 MPa.

2.3 Coatings characterisation

Surface and cross-sectional morphology observation of the as-deposited PEO coating, as-deposited duplex chameleon/PEO coating and fretting wear scars were explored using scanning electron microscopies (SEM) - Zeiss Ultra 55 (FEG-SEM), FEI Magellan HR (FEG-SEM) and Tescan Mira3 (FEG-SEM), all equipped with energy-dispersive X-ray (EDX) analysis facilities. A FEI Quanta 3D equipped with a focussed ion beam (FIB) facility was employed to prepare a cross-section of the duplex coating, avoiding the detrimental effects of mechanical polishing on the integrity of the interface. A trench of about 40 μm width and 30 μm depth was milled using an accelerating voltage of 30 kV, with currents of 65 and 15 nA for rough milling. Ion currents of 5 and 0.3 nA were then used for final polishing. To prevent surface charging and improve the conductivity of the specimens, a carbon layer about 10 nm thick was sputtered on all SEM samples.

Phase composition of the as-deposited chameleon/PEO coated sample and the wear scars were analysed using X-ray diffraction (XRD). A Rigaku SmartLab instrument 3kW with Cu $K_{\alpha1}$ (λ= 0.1542 nm) was employed at a scanning rate of 0.01°/min over the 2θ angular range of 10° to 120° at a grazing angle of 3°. The XRD machine was aligned and calibrated against a pure silicon cylinder before each measurement. 0

Nanoindentation testing was performed on the coatings with a Hysitron Ti950 instrument with a Berkovich diamond indenter. The duplex coating cross-sections were first prepared by mechanical grinding with up to 4000 grit sandpapers followed by polishing with up to 0.25 μm diamond pastes. Two hundred indents were made distributed across the whole coating thickness with 50 nm maximum indent depth and 10 s dwell time.

Surface roughness of the as-deposited duplex coating, PEO coating and wear scars was evaluated using a Keyence X200K laser confocal microscopy profilometer. Double scanning with 10% ND filter was used to maximise signal-to-noise ratio and evaluate the surface baseline and the apparent volume of the wear scar which was determined using methodology described in [27]. Based on the latter values and corresponding displacement amplitudes, nominal wear coefficients were then derived for the given number of fretting cycles and normal load applied during the tests.

Raman spectra of the duplex coatings and wear scars were collected using Renishaw System 1000 instrument with an Argon-ion laser (λ = 514.50 nm) as the excitation source. During the experiments, 30 s exposure times in the 200-1800 cm^{-1} spectral range were set. The instrument was calibrated against Si peak (520 cm^{-1}) of a pure silicon wafer before each measurement. The Raman spectra were taken from several 1 μm^2 size areas positioned within the wear scars and the as-deposited duplex coating with an in-situ optical microscope. The intensity ratio of E^1_{2g} and A_{1g} peaks located respectively at about 383 cm^{-1} and 408 cm^{-1} were utilised to account for the content of the basal and edge-plane MoS_2 crystals which could further stand for the crystallisation of the MoS_2 after the wear tests [39].

The average size of in-plane crystallite size L_a (nm) in graphite represents the graphitisation degree of the graphite in the top chameleon coating and is derived from the intensity ratio of D and G peaks (I_D/I_G) by the following equation [40, 41]:

$$L_a\ (nm) = (2.4 \times 10^{-10})\lambda^4 (\frac{I_D}{I_G})^{-1}$$

Where L_a (nm) is the average size of sp^2 crystallite clusters in graphite, I_D/I_G is the intensity ratio between the D and G peaks located respectively at around 1355 cm^{-1} and 1580 cm^{-1}, and λ (nm) is the excitation laser wavelength.

3. Results and discussion

3.1 Morphology and chemical composition of as-deposited coatings

SEM micrographs in Fig. 1a demonstrates a surface morphology typical of PEO coatings on Al alloys [9, 42]. A large number of micro-pores and micro-cracks can be observed within the surface. The micro-pores result from gas bubbles generated during the deposition process and the micro-cracks from the temperature gap and thermal stress between molten oxides and cold electrolyte [43]. In contrast, the chameleon-topped duplex coating (Fig. 1b) shows a compact and smooth appearance with grain-like structures across the surface. Several tens of microns long micro-cracks and visible thickness variations are also observed. Debris detached from the surface of the chameleon coating can be found around the grain-like structure boundaries (inset in Fig. 1b). The surface roughness evaluated by a laser confocal microscopy yielded values of $R_a = 2.5 \pm 0.5$ μm for the as-deposited PEO coating. After being burnished with chameleon topcoat layer, the surface roughness decreased to $R_a = 0.5 \pm 0.2$ μm.

Oxide layers formed via PEO typically exhibit a bilayer structure comprising a porous external layer and a denser internal layer [1, 2], which thickness ratio may vary in a wide range. In our case, the inner dense region was about 80 % of the overall PEO coating thickness as determined from the sample cross-section prepared by the standard metallographic polishing technique (Fig. 1c). The 2-3 μm thick outer porous layer exhibited large amounts of open micro-pores as can also be observed in Fig. 1a. This porous structure acts as a reservoir for the chameleon coating mixture which fills in these surface pores and provides a good adhesion of the top chameleon layer to the underlying PEO coating. In turn, the dense internal layer prevents any further penetration of the chameleon mixture and helps to keep its lubrication properties concentrated within the top of the duplex coating.

Lateral cracks were observed deep within chameleon solid lubricant layer, which could be caused by both burnishing process and sample preparation by polishing. Another cross-section was therefore prepared using FIB milling techniques (Fig. 2) in order to observe the chameleon/PEO interface and study the affected region. The milling location was chosen across the grain-boundary like feature of the chameleon coating (Fig. 2a). The surface morphology visible near the surface was caused by the ion beam damage. The presence of lateral cracks was confirmed within the chameleon layer, originating from the surface near the grain-boundary features (Fig. 2b) and indicating that they are likely to be caused by shear stress introduced during the burnishing process. The thickness of the burnished chameleon coating was 6.7 ± 1.6 μm and that of the PEO coating was 20.3 ± 0.5 μm. These estimates were consistent when assessed from the measurements on the FIB section (Fig. 2b) as well as from standard metallographic cross-sections prepared by mechanical polishing (Fig 1c).

The cross-sectional elemental distribution of Al, O, Si, Mo, S, Sb and C (Fig. 2c) shows a detail of the chameleon/PEO coating composition. The Al signal in Fig. 2c represents the distribution of Al_2O_3 and the PEO coating extent. Oxygen, whilst generally following the Al distribution in the lower part of the map, also continues in the top chameleon layer, reflecting the presence of Sb_2O_3 in it. The distribution of graphite could not be clearly determined due to the relatively low atomic mass and the unavoidable presence of adventitious carbon. In spite of the porosity (size <1 μm) the elements originating from the chameleon mixture have reached a uniform lateral distribution. The EDS elemental mapping furthermore reveals a re-distribution of MoS_2 and Sb_2O_3 across the layer (Fig. 2c). Sb, representing Sb_2O_3, is more concentrated near the chameleon/PEO interface, while the Mo and S of MoS_2 are mostly confined to the upper region of the chameleon coating. A similar distribution, with superficial MoS_2 and a deeper Sb_2O_3–rich layer, was reported in the previous research evaluating the commercial 40 % Sb_2O_3 - 60 % MoS_2 films on 440 C stainless steel substrates [44]. The Mo- and S- depleted regions, triangular in shape, are furthermore populated by Si-rich particles which might have been embedded during the coating deposition or the sample preparation process.

3.2 Crystal structure and mechanical properties

Fig. 3 shows the X-ray diffraction patterns for the as-deposited PEO and duplex coatings. The PEO coating material can be identified as a mixture of crystalline α/γ-Al_2O_3, with γ-Al_2O_3 being the dominant phase according to relative peak intensities. Some minor metallic Al diffraction peaks are observed, and are believed to stem directly from the substrate. This explanation is supported by the rough penetration depth evaluation in the HighScore Plus software using compact alumina for the simulation, while the depth was given out as between 22 and 40 µm, i.e. thicker than the duplex chameleon/PEO coating. Moreover, as opposed to the ideal compact alumina, the underlying porous PEO coating would allow a larger penetration depth in the duplex coating.

The X-ray diffraction pattern of duplex coating demonstrates the presence of hexagonal MoS_2 (main peak at 14°) and cubic Sb_2O_3 (at 27° and 32°) phases. The former shows a (002) preferred orientation with easy-shearing basal planes located parallel to the sample surface; the latter does not appear to have any preferred orientation, which could be due to a higher stiffness of the cubic structure of Sb_2O_3, featuring less separated easy-shearing planes. Al and α/γ-Al_2O_3 peak patterns originating from the underlying PEO coating and Al alloy substrate are also identified. No graphite signal is observed in the XRD pattern, suggesting that the carbon in the as-deposited chameleon layer may not form a specific crystalline structure with crystal sizes detectable by XRD.

The values of hardness and Young's modulus for PEO and duplex chameleon/PEO coatings evaluated by nanoindentation are summarised in Table 1. The results demonstrate that the hardness and Young's modulus of PEO coating are noticeably higher than that of the duplex chameleon/PEO coating. This is consistent with the presence of α-Al_2O_3 in the PEO layer, and the coating's intrinsically high microporosity which is a known source of significant variation seen in both hardness and elastic modulus data [9]. The duplex coating displays a lower composite hardness and stiffness, which can be linked to the presence of the chameleon top layer comprising soft phases, such as graphite, MoS_2 and Sb_2O_3. The high variability in elastic modulus of the duplex coating might owe to the embedded Si-rich particles (Fig. 2c). The cross-section hardness of the duplex coating is confirmed to be relatively low, as expected for the solid lubricating material on its surface.

3.3 Tribological behaviour

3.3.1 Critical transition conditions of the stick slip, partial slip and gross slip regimes

The volume loss was measured to assess the fretting wear behaviour at each fretting regimes obtained by the varying displacement amplitudes against the steel ball in humid air environment. The results are summarised in the fretting map (Fig. 4), along with derived nominal wear coefficient and corresponding graphite crystallite size, L_a (Raman spectra used for calculation are discussed in Section 3.4.2) for each displacement.

Three characteristic fretting regimes can be distinguished in the map (Fig. 4), as confirmed by fretting loops (Fig. 5), wear scars and corresponding wear depths. (Fig. 6): (i) stick at ~3 µm amplitude; (ii) partial slip in the 5-10 µm amplitude range and (iii) gross slip at amplitudes >10 µm. There is limited wear in stick regime and accordingly a low volume loss is observed (Fig. 6a). Partial slip appeared with amplitudes reaching 5 µm (Fig. 6b). The distinctive central stick zone with surrounding slip annulus can be observed in the scars, becoming more pronounced at 10 µm amplitude (Fig. 6c). Above 10 µm and up to around 80-100 µm, the fretting is in the gross slip regime. Full slide occurs in the gross regime, where wear debris appear on the surfaces (Fig. 6d and 6e). Debris generation is more evident at larger fretting amplitudes and they visibly accumulate at the wear scars' edges. Average scar depths increase with displacement amplitude (Fig. 6f) up to a maximum of 3 µm which is less than the mean average thickness of chameleon layer, 6.7 µm. However relatively large scatters of both values imply that under high displacement amplitudes, ridges of underlying PEO coatings may become exposed, affecting the wear of chameleon coating.

Despite the fact that increases in the scar depth slow down at displacements ≥20 µm, the wear volume increases steadily from ~10^{-5} to ~4×10^{-4} mm^3 throughout the whole range of displacement amplitudes (Fig. 4). It appears that at greater displacements, the wear volume becomes additionally contributed by widening the scar, which is indicative of progressive development of the steel ball wear in the gross slip regime [19]. However, the nominal wear coefficient of the duplex coating does not follow this trend, while exhibiting a maximum at the 20-µm displacement. When operating in terms of the nominal wear coefficient, it should be noted that the sliding distance is increasingly overestimated towards lower displacement magnitudes [20], so the actual wear coefficient becomes underestimated accordingly, and the maximum wear rate would be likely to correspond to a lower displacement. Such behaviour in the partial slip regime is inconsistent with [19] and resembles that of lubricated fretting contacts [45, 46], where it is commonly attributed to the increased coefficient of friction due to lubricant starvation regime developed at displacements corresponding to the stick-slip mode under dry fretting conditions [47, 48]. However, lubricant starvation is unlikely situation in the case of a solid lubricant which is always present in the contact zone. A plausible explanation to this controversy can be found considering a correlation which can be traced between the wear coefficient and the in-plane crystalline size (L_a) of graphite in the matrix of chameleon layer, which decreases from 17.6 to 14.8 nm when displacement amplitude increases from 3 to 100 µm (Fig. 4). Noticeably, a region of displacement magnitudes ≤10 µm where the increased wear occurs is likely to coincide with a rather gradual increase in the defect density of graphite basal planes. Beyond that, at amplitudes ≥40 µm, wear minimises when L_a values become as low as in the burnished chameleon layer (represented by the dashed line at 15.15 nm in Fig. 4) and practically independent of displacement. This indicates that at intermediate displacements (10 to 40 µm), shear between basal planes of graphite is activated, which results in a reduced wear. This may to an extent be affected by rotation and shear of MoS_2 grains in graphite matrix, however existing evidence is insufficient to made definitive judgements on the significance of this effect. Thus graphite appears to offer beneficial lubrication and wear reduction in the gross slip regimes, the transition to which is facilitated by the application of the solid lubricant chameleon layer.

It is also important to note that amplitudes of transitions to stick and stick-slip regimes (most detrimental regimes for contact fatigue) summarised in Fig. 4, were reduced by about an order of magnitude for the chameleon/PEO coating as compared to single layer PEO coating, which showed about 42 μm onset of stick regime and 56 μm onset of stick-slip regime from earlier reported tests against steel ball under similar contact pressures in air [27].

3.3.2 Fretting wear behaviour in gross slip regime

With an amplitude set at 100 μm, the fretting behaviour is fully in the gross slip regime. The coefficient of friction (CoF), or tangential force to load ratio, was measured for the PEO and the duplex chameleon/PEO coatings under 20 N load against alumina balls in N_2 and air, for 10^4 cycles as shown in Fig. 7. The CoF variation data is originally coming from our previous work [27].

The CoFs of PEO coating in both nitrogen and air are much higher than those of duplex chameleon/PEO coatings. By adding a chameleon top layer, the CoF is reduced from about 0.88-0.92 to 0.07-0.09 in N_2 and from 0.58-0.62 to 0.10-0.12 in air. Such reduction in CoF on duplex coatings is linked to the known lubrication properties of the top graphite/MoS_2/Sb_2O_3 chameleon coating. For the single layer PEO coating, the lower CoF in air as compared to that in dry N_2, can be explained by the formation of a thin aluminium hydroxide lubricating film between the interface of the alumina counterpart and the PEO coating [42]. The CoF behaviour in identical conditions against steel counterparts in air is shown in Fig. 8, along with an additional fretting test as a lower 15 N load on the duplex coating.

The CoF exhibited by the PEO coating is generally much higher than that of the duplex chameleon/PEO coating, just like in conditions described previously for alumina counterpart. However, under a 20 N load the CoF of the duplex coating shows a sharp increase against the steel ball in air after about 6×10^3 testing cycles. The CoF values are stable until that stage, at 0.11-0.12, yet raise by factor of close to 4 to about 0.40-0.41 by 10^4 cycles and the end of the test. Generation and accumulation of debris between the sliding surfaces described in the previous section might augment contact stresses and explain this increasing trend in CoF values for steel counterparts [26].

At the lower 15 N load, the CoF also exhibits fluctuating values, but the onset is at the later stage of 8×10^3 cycles and the increase is significantly more limited, from 0.1 to 0.15 approximately (Fig. 8).

3.4 Characteristics of the wear scars

3.4.1 Surface topography

Laser confocal microscopy images of surface topography of wear scars produced after 10^4 fretting cycles in the gross slip mode, at 100 μm amplitude, are shown in Fig. 9-13 (with upper and lower parts showing respectively unfiltered and filtered topology images, as described in Section 2.3), together with corresponding SEM images and EDS maps of the main chemical elements, whereas the total values of volumetric wear are summarised in Table 2.

The data of Table 2 indicates that under 20 N normal load, the two scars produced against steel exhibit relatively large volume losses comparing to those produced against alumina. With steel counterparts, the cumulative volume loss of the scar tested in N_2 ((13.94 ± 0.08) $\times 10^{-4}$ mm^3) appears larger than in air ((7.92 ± 0.40) $\times 10^{-4}$ mm^3). In contrast, the two scars produced against alumina balls exhibit smaller volume losses in N_2 ((1.41 ± 0.18) $\times 10^{-4}$ mm^3 than in air ((4.98 ± 0.09) $\times 10^{-4}$ mm^3). Furthermore, volume loss of the scar produced under a lower 15 N load ((4.73 ± 0.06) $\times 10^{-4}$ mm^3) is less than those tested under 20N in air ((7.92 ± 0.40) $\times 10^{-4}$ mm^3) and in N_2 ((13.94 ± 0.08) $\times 10^{-4}$ mm^3) with the same counterpart material.

Surface topographies of wear scars produced against alumina (Fig. 9 and 10) show smaller wear volume than in the case of steel counterparts (Fig. 11 and 12). Smooth structures with less debris could be observed in the scars tested with alumina balls. It is worth noting that the presence of Al in those two scars may be a mixed contribution of the underlying layers, and wear debris from the alumina counterpart balls. The top chameleon layer shows minor stripping in both scars, similar to the damage found in the wear scar produced against steel under a lower 15 N load (Fig. 13).

Compared to the wear scars produced with the alumina ball under 20 N load, scars produced against steel balls show much more complex and disordered wear patterns when the fretting wear test was conducted in air (Fig. 12a) and in N_2 (Fig. 11a). The corresponding SEM/EDS images indicate that the chameleon coating was almost entirely removed from the contact area in the former case, and large amounts of entrapped debris appear at the surface of the scar. The debris dark-brown in colour is composed mainly of iron oxide and alumina, which may originate from oxidation of the counterpart steel and from the underlying alumina PEO coating. This may have led to underestimation of the actual coating volume loss reported in Table 2. The wear profile along the sliding direction (Fig. 12a) further substantiates the existence of wear debris in the scar, supporting the debris-based interpretation of irregular CoF increases observed in Fig. 8. Meanwhile, the abnormal CoF indicated that even with severe fretting damage to the top chameleon layer, parts of it entrapped in the outer porous region of PEO coating still offer lubrication properties and the duplex coating retains its protective function.

Surface topography shows that significantly smoother scars are produced under lower normal loads in air and against steel counterparts (15 N, Fig. 13a,b *vs* 20 N, Fig. 12a,b). The corresponding SEM images and EDS maps indicate that the top chameleon layer was partially removed from the contact area even at the lower load. Strong Al signal on the surface further shows that the underlying PEO alumina is exposed where the chameleon top layer was stripped off the coating by fretting wear after 10^4 cycles. Some minor distribution of Fe could also be found in the EDS maps, possibly originating from the steel counterpart. These elemental distributions are consistent with debris from both the duplex coating and the steel counterpart participating in the increases in CoF reported in Fig. 8.

It could therefore be concluded that the duplex coating offers better lubrication properties against steel counterparts in N_2 than it does in air. The humidity of air environments and high normal load of 20 N corresponding to 1.1 GPa initial contact Hertzian pressure, can both be expected to significantly affect the lubrication performance of the chameleon coating and to result in severe surface damage and coating failure in the contact area. On the other hand, the tribological performance of the duplex coating under 15 N load corresponding to about 0.96 GPa initial contract Hertzian pressure, indicates improved lubrication properties in fretting conditions. One of the key factors impacting coating performance negatively is therefore normal load, with an oxidising environment further precipitating failure of the chameleon top layer.

3.4.2 Structural rearrangements in the surface layer

The XRD patterns obtained from within wear scars generated on duplex coatings at 100 µm fretting amplitude are presented and compared to the pre-test surface condition in Fig. 14. All wear scars exhibit hexagonal MoS_2 (main peak at 14°) and cubic Sb_2O_3 (main peak at 27° and 32°) phases. While the overall XRD patterns are generally similar, the intensities of Al (37°, 45°, 65° and 78°) and Al_2O_3 (46° and 67°) peaks exhibit changes in the XRD patterns. The scar produced against the steel ball in air, in particular, shows higher intensities for Al peaks.

Raman spectra of fretting wear scars produced under 20 N load and of the as-deposited duplex chameleon/PEO coating are shown in Fig. 15. Two characteristic Raman active peaks for crystalline MoS_2 (E^1_{2g} 383 cm^{-1} and A_{1g} 408 cm^{-1}) are clearly present in the data, where the E^1_{2g} and A_{1g} symmetries represent in-plane S-Mo-S and out-of-plane S phonon modes, respectively [39]. The wider D and G bands characteristic of graphite also predictably appear at around 1355 cm^{-1} and 1580 cm^{-1}, respectively. Two characteristic peaks for Sb_2O_3, which would be expected at about 230 cm^{-1} and 450 cm^{-1}, could not be detected in the spectra. Some minor Sb_2O_3 peaks (at about 220 cm^{-1} and 600 cm^{-1}) are however present indicating that the compound is present yet not in crystalline form [44].

A number of weak peaks appear, at about 290 cm^{-1}, 460 cm^{-1}, 920 cm^{-1} and 1620 cm^{-1}. The first two might be a secondary Raman response of MoS_2, with different phonon modes, and the 1620 cm^{-1} peak could be attributed to a similar lattice vibration of G peak. The signal peak at 920 cm^{-1} appears only after the fretting test against steel counterpart in air. This particular peak could not be clearly identified; it might originate from the presence of oxides and other compounds after fretting test [49, 50].

More striking differences in the Raman data lie in the variation in relative intensities of the main four peaks described above. Typical crystallite size L_a can be derived from the corresponding ratio for graphite as described in the experimental section and used for fretting wear regime comparisons in Fig. 4. For MoS_2, the peak intensity ratio of in plane E^1_{2g} and out of plane A_{1g} peaks can be used to track crystallisation of MoS_2 with base planes parallel to the wear surface. The results of such analysis are summarised in Table 3.

From Table 3, E^1_{2g}/A_{1g} ratio is found above 0.88 on all samples, indicating a relatively high crystallisation of MoS_2 and good alignment along the basal planes. Scars produced in nitrogen show about 2% higher MoS_2 plane alignment than those under humid air, with the highest overall produced against steel counterpart. The scar produced against alumina in air yielded the lowest observed MoS_2 E^1_{2g}/A_{1g} ratio (0.88), in the conditions where graphite crystallite size is high, allowing for a relatively straightforward interpretation. Water adsorption and oxidation in humid air conditions promotes stripping of superficial MoS_2, exposing the MoS_2 film experienced an unfavourable friction condition and would be replaced by the graphite film. The graphite film would gradually cover the wear scar and got highly crystallised during the fretting test.

The re-alignment of the in-plane graphite appeared induced by the fretting wear tests, resulting in the graphite crystallite size (L_a) of each tested scars increasing from 15.15 nm to about 16.00 nm in nitrogen and 17.60 nm in air. One reduced value exception could also be observed in the scar tested against steel in N_2. As with wear tests in air, due to the continuous consuming of the intercalating water molecules in N_2, the outer graphite film gradually disintegrated during the friction contact and was replaced by the MoS_2 film.

As observed by laser confocal profilometry (Fig. 9-13), parts of top chameleon coating is pushed away from the contact area by fretting, and wear debris accumulates locally within the scars. The cumulated debris is particularly apparent in scars produced in air, for which Raman spectroscopy results are shown in Fig. 16.

The Raman spectrum of the scar produced against alumina in air (Fig. 16a) shows an additional minor peak at approximately 252 cm^{-1}, for which aluminium hydroxide $Al(OH)_3$ is the most probable candidate (expected shift of 240-257 cm^{-1}) [51]. Although formation of hydroxide tribolayer has been previously reported to have beneficial effect on CoF of PEO alumina against Al_2O_3 [42] (see Section 3.3.2), in the case of duplex chameleon-PEO coating, wear debris are dominated by constituents of chameleon layer which appears to have the major influence on its fretting behaviour. The Raman spectrum of the debris in the scar produced against steel in air (Fig.16b) exhibits no trace of the hexagonal MoS_2 in between 250-550 cm^{-1} Raman shift while the graphite shows relatively amorphous state with low graphitisation degree. More peaks appeared at approximately 215cm^{-1}, 287cm^{-1} and 403cm^{-1}, which can be attributed to iron hydroxide (FeO(OH)) [52] and at 452cm^{-1} and 635cm^{-1}, which corresponds to chromium hydroxide (CrO(OH)) [53]. The iron and chromium contents can be linked to the 440 steel counterpart, their oxides/hydroxides forming in the humidity of the air environment. The accumulating of such FeO and CrO containing debris can be then linked to the dramatic increase in CoF after 6×10^3 cycles (Fig. 8) and to stripping of the chameleon topcoat under fretting wear against steel counterparts at 20 N (about 1.1 GPa) test (Fig. 12). In this case, the presence of graphite proves insufficient for proper lubrication during the fretting test at such environment and load conditions.

3.4.3 Sub-surface layer evolution

The cross-sections of the gross-slip fretting wear scars produced under 20 N load and 100 μm displacement amplitude after 10^4 cycles were mechanically prepared and observed by SEM in the backscattered electron mode. To investigate material integrity in the region of tensile stress distribution, images were captured at the edges of the scars, along the fretting direction (Fig. 17-20).

The chameleon topcoat is severely affected by fretting as deducted from the experiments after 10^3 cycles under 100 μm displacement amplitude. With friction increased at the later stage of the test, a simultaneous generation of wear debris and crack propagation was observed indicating a competition between the fretting wear and fretting fatigue processes. Figs. 19 and 20 show long micro-cracks (around 10 to 18 μm in length) and worn surfaces in the contact area indicating that steel counterparts can strip the chameleon topcoat locally and result in catastrophic failure in the underlying PEO coating. In a single investigated area (40-50 μm in length and 40-45 μm in width) of the sample tested against steel in air, the damage was also observed in the Al alloy substrate (Fig. 20c) Closer observation of this unique area (Fig. 20d) highlights the generation of fatigue cracks in the Al alloy at the depth of 40-60 μm from the surface, corresponding to the location of the maximum contact shear stress in the steel/PEO-alumina couple. Micro-pores are observed along those cracks and are believed to have cause further damage in the substrate. The origin of this fatigue cracking affected area might lie in high tangential stress displacements at the edge of the wear scar (partial stick-slip zone) developed when the chameleon layer wore out and the friction coefficient increased. Moreover, due to damage in the integrity of PEO layer, the development of fatigue cracks in the Al alloy substrate might be further accelerated by oxidation during the fretting tests in air.

Crack initiation due to repetitive fretting wear is shown schematically in Fig. 21. Two different types of cracks appear in the scar produced against steel in N_2 (Fig. 19). The first oblique propagation crack might be caused by tangential stress during the repetitive fretting contacts. Due to high shear stresses within the fretting wear scar, these oblique cracks tend to occur at the edges of the scars. As shown in Fig. 18a and 19a, such cracks grow obliquely in the PEO coating at angles between 40° and 45° to the surface. The vertical cracks, in turn, likely stem from tensile stress due to the volume straining of the PEO coating on Al alloy under the contact load, where some elastic compliance of the underlying aluminium alloy may lead to the repeated stress accumulation within the PEO layer. In reciprocating fretting wear, the occurrence of vertical cracks relaxes surface tensile stresses and more cracks would be initiated along the fretting contact areas, as shown in Fig. 20a. Owing to high loading and tangential stresses within the forming fretting scars, vertical cracks tend to penetrate through the entire PEO coating and reach the underlying substrate, resulting in fatigue cracks in the Al alloy (Fig. 20a,c).

In scars produced against alumina balls, few oblique cracks can be observed in the underlying PEO coating and the cracks induced are shorter at 4 to 8 μm in length in both N_2 and air (Fig. 18a). The collapse of micro-pores in the PEO coating developed into some larger cavities (Fig. 17b and 18b), however there were no penetration cracks to the underlying substrate form those fatigue sites in the PEO layer.

The cross-section of the scar produced against the steel ball in air under 15 N load also shows partial removal of the chameleon topcoat (Fig. 22). Some micro-cracks and minor micro-pores can also be observed in the underlying PEO coating (Fig. 22a,b). Induced crack lengths range from 7 to 8 μm and are significantly shorter than those produced at a larger 20 N load (10-18 μm). Again the selection of the appropriate loading condition is critical, where high contact pressures (such as $\sim$1.1 GPa at 20 N load on the steel ball) can be detrimental for the coating performance.

In summary, the duplex chameleon/PEO coating offers improved lubrication under 15 N load against steel in air, while it failed to provide continuous lubrication under 20 N load, where the coating would experience large wear damage and eventually break down in the contact area with fatigue crack initiation and propagation into the underlying substrate. In contrast, a more inert alumina counterpart shows comparatively limited negative impact on the duplex coating. This allows the following generalisation to be made, which emphasises the importance of both interfacial engineering and third-body behaviour in the fretting performance of the duplex-coated Al components under high contact loads. With the material of the top chameleon layer being prone to easy shearing and quick displacement, the porous outer region of the underlying PEO coating plays crucial role in its retention in the contact zone. However, once the PEO coating ridges become exposed, the third body behaviour comes into play. In situations where the counterface is prone to oxidative wear (e.g. during fretting against steel ball in humid air) and oxide debris are retained in the surface (e.g. due to adhesive interaction between Fe/Cr oxo-hyroxides and PEO alumina), friction increases so as energy dissipated in the surface layer. If the contact pressure is sufficiently high, this will lead to the development of fatigue cracks in the PEO layer and ultimately to the oxidative fatigue of the metal substrate – that is the system behaviour is reverted from gross-slip lubricated fretting wear to the partial-slip unlubricated fretting fatigue. However, if the energy dissipation is reduced (e.g. by eliminating factors leading to the high friction, lowing the contact pressure or displacement amplitude) this would result in a steady-state fretting performance of the composite layer with reduced wear and minimised risk of fatigue.

4. Conclusions

Detailed investigation of the behaviour of duplex chameleon/PEO coatings on an Al alloy substrate in fretting wear tests against different counterparts (steel and alumina) and in different environments (humid air and dry nitrogen) has resulted in the following conclusions:

(1) The specific stick, partial slip and gross slip regimes were observed as amplitudes increasing from 3 to 100 μm. At 3 μm amplitude, a small ring of damaged stick zone could be observed in the fretting area. A distinctive annular slip zone then appeared in the fretting scars, and the small circular stick region grew much larger as the amplitude increased from 5 to 10 μm. Further increases in amplitude resulted in full gross sliding with no central stick zone. As compared to the previously studied single layer PEO coating [27], the critical transitions to fatigue prone regimes of stick and stick-slip were reduced by about an order of magnitude for duplex chameleon/PEO coating.

(2) A humid air atmosphere was found to increase the crystallisation degree of graphite while a dry nitrogen environment could enhance the re-orientation of MoS_2 basal planes. This allowed graphite and MoS_2 to confer their self-lubrication properties to the surface during the fretting tests. The results identified the adaptive mechanisms of the chameleon coating integrated with the hard PEO layer.

(3) The change in the crystalline size of graphite was correlated with the increase in the wear rate of the duplex coating observed during fretting in the partial slip regime against steel in humid air, which is at odds with some common views on unlubricated fretting [19] and cannot be explained by the lubricant starvation effect observed in liquid-lubricated contacts. It is proposed that the increased coating wear is associated with damage accumulation in graphite basal planes when stick prevails, whereas reduction of wear in the gross slip mode is triggered by activation of shear between basal planes of graphite at displacement amplitudes between 10 and 40 μm.

(4) Steel counterparts were found generally to induce more severe wear and higher CoF during fretting than alumina, especially in humid air conditions. This was linked to the formation of iron and chromium oxides/hydroxides containing debris and severe abrasion at contact pressures above 1 GPa. The debris accumulated in the contact zone led to rising CoF values, which induced an accelerated growth of long penetration micro-cracks in the PEO coating, ultimately resulting in the oxidisation of the aluminium substrate. At the same time for contact pressures below 1 GPa, the duplex coating showed good lubrication properties with limited generation of micro-cracks and micro-pores in the PEO coating. The normal load therefore appears to be the key factor in catastrophic coating failure, with a humid atmosphere further downgrading performance in fretting wear due to oxidation.

(5) Both oblique and vertical grown cracks were observed in the fretting scars after 10^4 cycles. Tangential stress might have initiated the former, before they turned to tilted-grown with an angle of about 40-45° upon reaching the PEO coating. Vertical cracks are thought to result from tensile stress and tended to grow vertically into the PEO coating as well, leading to its failure and

to severe oxidation of the Al alloy substrate. Such fatigue crack appearance was absent for tests when the load was reduced from 20 N to 15 N.

Overall, this work has demonstrated that a duplex chameleon/PEO coating can effectively decrease fretting CoF and wear in the gross-slip regime and dramatically improve fretting wear resistance over a simple PEO coating through the observed self-adaptation and wear mechanisms when a proper consideration is given to the combination of normal load, environment and counter body.

Acknowledgements

This work was supported by the European Research Council under the ERC Advanced Grant (320879 ‘IMPUNEP’) and ERC-2018-PoC programme (825122 - 3D Cer-Met). The authors would like to thank Yanfei Liu from Harbin Engineering University, China, for the help with the fretting sliding tests.

References

[1] Du KQ, Guo XH, Guo QZ, Wang Y, Wang FH, Tian Y. Effect of PEO Coating Microstructure on Corrosion of Al 2024. J Electrochem Soc. 2012;159:C597-C606.

[2] Nie X, Leyland A, Song HW, Yerokhin AL, Dowey SJ, Matthews A. Thickness effects on the mechanical properties of micro-arc discharge oxide coatings on aluminium alloys. Surface and Coatings Technology. 1999;116-119:1055-60.

[3] Kear BH, Kalman Z, Sadangi RK, Skandan G, Colaizzi J, Mayo WE. Plasma-sprayed nanostructured Al2O3/TiO2 powders and coatings. Journal of Thermal Spray Technology. 2000;9:483-7.

[4] Staia MH, Puchi Cabrera ES, Iost A, Zairi A, Belayer S, Van Gorp A. Tribological response of AA 2024-T3 aluminium alloy coated with a DLC duplex coating. Tribology International. 2015;85:74-87.

[5] Baragetti S, Lusvarghi L, Bolelli G, Tordini F. Fatigue behaviour of 2011-T6 aluminium alloy coated with PVD WC/C, PA-CVD DLC and PE-CVD SiOx coatings. Surface and Coatings Technology. 2009;203:3078-87.

[6] Li Q, Liang J, Liu B, Peng Z, Wang Q. Effects of cathodic voltages on structure and wear resistance of plasma electrolytic oxidation coatings formed on aluminium alloy. Applied Surface Science. 2014;297:176-81.

[7] Nie X, Meletis EI, Jiang JC, Leyland A, Yerokhin AL, Matthews A. Abrasive wear/corrosion properties and TEM analysis of Al2O3 coatings fabricated using plasma electrolysis. Surface and Coatings Technology. 2002;149:245-51.

[8] Huang Y, Shih H, Huang H, Daugherty J, Wu S, Ramanathan S, et al. Evaluation of the corrosion resistance of anodized aluminum 6061 using electrochemical impedance spectroscopy (EIS). Corrosion Science. 2008;50:3569-75.

[9] Yerokhin AL, Shatrov A, Samsonov V, Shashkov P, Pilkington A, Leyland A, et al. Oxide ceramic coatings on aluminium alloys produced by a pulsed bipolar plasma electrolytic oxidation process. Surface and Coatings Technology. 2005;199:150-7.

[10] Tian J, Luo Z, Qi S, Sun X. Structure and antiwear behavior of micro-arc oxidized coatings on aluminum alloy. Surface and Coatings Technology. 2002;154:1-7.

[11] Rogov AB, Yerokhin A, Matthews A. The Role of Cathodic Current in Plasma Electrolytic Oxidation of Aluminum: Phenomenological Concepts of the “Soft Sparking” Mode. Langmuir. 2017;33:11059-69.

[12] Rogov AB, Matthews A, Yerokhin A. Role of cathodic current in plasma electrolytic oxidation of Al: A quantitative approach to in-situ evaluation of cathodically induced effects. Electrochimica Acta. 2019;317:221-31.

[13] Berthier Y, Vincent L, Godet M. Fretting fatigue and fretting wear. Tribology International. 1989;22:235-42.

[14] Endo K, Goto H. Initiation and propagation of fretting fatigue cracks. Wear. 1976;38:311-24.

[15] Mall S, Jain V, Fadag H. Effects of Shot‐Peening on Fretting Fatigue Crack Growth Behavior in Ti‐6Al‐4V. Strain. 2011;47:e305-e18.

[16] Low M. Fretting problems and some solutions in power plant machinery. Wear. 1985;106:315-35.

[17] Pearson B, Brook P, Waterhouse R. Fretting in aqueous media, particularly of roping steels in seawater. Wear. 1985;106:225-60.

[18] Géringer J, Kim K, Boyer B. Fretting corrosion in biomedical implants. Tribocorrosion of passive metals and coatings: Elsevier; 2011. p. 401-23.

[19] Vingsbo O, Söderberg S. On fretting maps. Wear. 1988;126:131-47.

[20] Pearson S, Shipway P. Is the wear coefficient dependent upon slip amplitude in fretting? Vingsbo and Söderberg revisited. Wear. 2015;330:93-102.

[21] Elleuch K, Fouvry S, Kapsa P. Fretting maps for anodised aluminium alloys. Thin solid films. 2003;426:271-80.

[22] Zhou Z, Vincent L. Mixed fretting regime. Wear. 1995;181:531-6.

[23] Hager Jr C, Sanders J, Sharma S. Characterization of mixed and gross slip fretting wear regimes in Ti6Al4V interfaces at room temperature. Wear. 2004;257:167-80.

[24] Paulin C, Fouvry S, Deyber S. Wear kinetics of Ti–6Al–4V under constant and variable fretting sliding conditions. Wear. 2005;259:292-9.

[25] Fouvry S, Kapsa P, Vincent L. An elastic–plastic shakedown analysis of fretting wear. Wear. 2001;247:41-54.

[26] Chapter 15 - Fretting and Minor Wear Mechanisms. In: Stachowiak GW, Batchelor AW, editors. Engineering Tribology (Fourth Edition). Boston: Butterworth-Heinemann; 2014. p. 647-77.

[27] Liu Y-F, Liskiewicz T, Yerokhin A, Korenyi-Both A, Zabinski J, Lin M, et al. Fretting wear behavior of duplex PEO/chameleon coating on Al alloy. Surface and Coatings Technology. 2018;352:238-46.

[28] Muratore C, Voevodin AA. Chameleon coatings: adaptive surfaces to reduce friction and wear in extreme environments. Annual Review of Materials Research. 2009;39:297-324.

[29] Sliney HE. Solid lubricant materials for high temperatures—a review. Tribology International. 1982;15:303-15.

[30] Voevodin AA, Zabinski J. Nanocomposite and nanostructured tribological materials for space applications. Composites Science and Technology. 2005;65:741-8.

[31] Voevodin AA, Zabinski J. Supertough wear-resistant coatings with 'chameleon'surface adaptation. Thin Solid Films. 2000;370:223-31.

[32] Baker C, Hu J, Voevodin A. Preparation of Al2O3/DLC/Au/MoS2 chameleon coatings for space and ambient environments. Surface and Coatings Technology. 2006;201:4224-9.

[33] Hu J, Muratore C, Voevodin AA. Silver diffusion and high-temperature lubrication mechanisms of YSZ–Ag–Mo based nanocomposite coatings. Composites Science and Technology. 2007;67:336-47.

[34] Krzanowski JE, Endrino J, Nainaparampil J, Zabinski J. Composite coatings incorporating solid lubricant phases. Journal of materials engineering and performance. 2004;13:439-44.

[35] Qin Y, Xiong D, Li J, Jin Q, He Y, Zhang R, et al. Adaptive-lubricating PEO/Ag/MoS2 multilayered coatings for Ti6Al4V alloy at elevated temperature. Materials & Design. 2016;107:311-21.

[36] Xiang Z-F, Liu X-B, Ren J, Luo J, Shi S-H, Chen Y, et al. Investigation of laser cladding high temperature anti-wear composite coatings on Ti6Al4V alloy with the addition of self-lubricant CaF2. Applied surface science. 2014;313:243-50.

[37] Zabinski J, Bultman J, Sanders J, Hu J. Multi-environmental lubrication performance and lubrication mechanism of MoS 2/Sb 2 O 3/C composite films. Tribology Letters. 2006;23:155-63.

[38] Liskiewicz T, Kubiak K, Comyn T. Nano-indentation mapping of fretting-induced surface layers. Tribology International. 2017;108:186-93.

[39] Tan SM, Ambrosi A, Sofer Z, Huber Š, Sedmidubský D, Pumera M. Pristine basal ‐ and edge ‐ plane ‐ oriented molybdenite MoS2 exhibiting highly anisotropic properties. Chemistry – A European Journal. 2015;21:7170-8.

[40] Tuinstra F, Koenig JL. Raman spectrum of graphite. The Journal of chemical physics. 1970;53:1126-30.

[41] Cançado L, Takai K, Enoki T, Endo M, Kim Y, Mizusaki H, et al. General equation for the determination of the crystallite size L a of nanographite by Raman spectroscopy. Applied Physics Letters. 2006;88:163106.

[42] Yerokhin A, Nie X, Leyland A, Matthews A, Dowey S. Plasma electrolysis for surface engineering. Surface and coatings technology. 1999;122:73-93.

[43] Li Q, Liang J, Wang Q. Plasma electrolytic oxidation coatings on lightweight metals. Modern surface engineering treatments. 2013;4:75.

[44] Zabinski J, Donley M, McDevitt N. Mechanistic study of the synergism between Sb2O3 and MoS2 lubricant systems using Raman spectroscopy. Wear. 1993;165:103-8.

[45] Haviez L, Fouvry S, Yantio G. Investigation of grease behavior under simple and complex displacement amplitudes conditions. Tribology International. 2016;100:186-94.

[46] Kalin M, Vižintin J, Novak S, Dražič G. Wear mechanisms in oil-lubricated and dry fretting of silicon nitride against bearing steel contacts. Wear. 1997;210:27-38.

[47] Shima M, Suetake H, McColl IR, Waterhouse RB, Takeuchi M. On the behaviour of an oil lubricated fretting contact. Wear. 1997;210:304-10.

[48] Zhou ZR, Vincent L. Lubrication in fretting—a review. Wear. 1999;225-229:962-7.

[49] Kolesov B, Geiger C. Raman spectra of silicate garnets. Physics and Chemistry of Minerals. 1998;25:142-51.

[50] Ferrari AM, Valenzano L, Meyer A, Orlando R, Dovesi R. Quantum-mechanical ab initio simulation of the Raman and IR spectra of Fe3Al2Si3O12 almandine. The Journal of Physical Chemistry A. 2009;113:11289-94.

[51] Huang E, Li A, Xu Ja, Chen RJ, Yamanaka T. High‐pressure phase transition in Al (OH) 3: Raman and X‐ray observations. Geophysical Research Letters. 1996;23:3083-6.

[52] De Faria D, Venâncio Silva S, De Oliveira M. Raman microspectroscopy of some iron oxides and oxyhydroxides. Journal of Raman spectroscopy. 1997;28:873-8.

[53] Yang J, Martens WN, Frost RL. Transition of chromium oxyhydroxide nanomaterials to chromium oxide: a hot‐stage Raman spectroscopic study. Journal of Raman Spectroscopy. 2011;42:1142-6.

Artwork Captions

Table 1. Hardness and Young's modulus of as-deposited PEO and duplex coatings.

Table 2. Volume losses of wear scars obtained on duplex chameleon/PEO coatings under different test conditions, as derived from laser confocal topography maps.

Table 3. MoS_2 E^1_{2g}/A_{1g} peak ratios reflecting degree of MoS_2 crystallization and in plane graphite crystallite sizes from the Raman spectra presented in Fig.15

Figure 1. Surface morphologies of PEO coating (a), duplex chameleon/PEO coating (b) and cross-sectional morphology of the duplex chameleon/PEO coating (c) studied in this work.

Figure 2. Cross-section of as-deposited duplex chameleon/PEO coating prepared by FIB milling technique: (a) location of the FIB milling on the coating surface observed as the stage tilt 30°; (b) coating cross section image; and (c) chameleon/PEO interfacial cross-section with elemental distribution maps.

Figure 3. X-ray diffraction patterns of as-deposited PEO and duplex chameleon/PEO coatings.

Figure 4. Fretting map of duplex chameleon-PEO coating on Al against steel counterpart in humid air showing dependencies of the volume loss, nominal wear coefficient and calculated in-plane crystalline size L_a of graphite phase in chameleon layer on displacement amplitude. The optical images of the five typical wear scars (a-e) are shown in Figure 6.

Figure 5. Typical examples of fretting loops for duplex chameleon-PEO coatings against steel in humid air in the partial (a) and gross (b) slip regimes.

Figure 6. Optical micrographs of scars obtained in wear tests of different amplitudes (a-e) and corresponding average wear depths (f).

Figure 7. Evolution of coefficient of friction for PEO and duplex chameleon/PEO coatings under 20 N against alumina balls in N_2 (a) and air (b) (adapted from [27]).

Figure 8. Evolution of coefficient of friction for PEO and duplex chameleon/PEO coatings under 15 N/20 N against steel balls in air.

Figure 9. Laser confocal topography (a) and SEM/EDS images (b) & (c) of the wear scar produced under 20 N load against an alumina ball in N_2 after 10^4 fretting cycles under 100 μm displacement amplitude.

Figure 10. Laser confocal topography (a) and SEM/EDS images (b) & (c) of the wear scar produced under 20 N load against an alumina ball in air after 10^4 fretting cycles under 100 μm sliding amplitude.

Figure 11. Laser confocal topography (a) and SEM/EDS images (b) & (c) of the wear scar produced under 20 N load against a steel ball in N_2 after 10^4 fretting cycles under 100 μm displacement amplitude.

Figure 12. Laser confocal topography (a) and SEM/EDS images (b) & (c) of the wear scar produced under 20 N load against a steel ball in air after 10^4 fretting cycles under 100 μm displacement amplitude.

Figure 13. Laser confocal observation (a) and SEM/EDS images (b) & (c) of the wear scar tested under 15 N load against steel ball in air after 10^3 fretting cycles under 100 μm displacement amplitude.

Figure 14. X-ray diffraction patterns obtained from within gross-slip fretting wear scars produced under 20 N loads, and of as-deposited duplex chameleon/PEO coating.

Figure 15. Raman spectra of the wear scars produced under 20 N loads and of as-deposited duplex chameleon/PEO coating.

Figure 16. Raman spectra of the accumulated debris in the scars produced in air under 20 N loads, (a) against steel ball; (b) against alumina ball for fretting wear of duplex chameleon/PEO coating.

Figure 17. (a), (b) Cross-section SEM images of the fretting wear scar produced on duplex chameleon/PEO coating under 20 N load against alumina ball in N_2 after 10^4 fretting cycles under 100 μm displacement amplitude.

Figure 18. (a), (b) Cross-section SEM images of the fretting wear scar produced on duplex chameleon/PEO coating under 20 N load against alumina ball in air after 10^4 fretting cycles under 100 μm displacement amplitude.

Figure 19. (a), (b) Cross-section SEM images of the fretting wear scar produced on duplex chameleon/PEO coating wear scar produced under 20 N load against steel ball in N_2 after 10^4 fretting cycles under 100 μm displacement amplitude.

Figure 20. (a), (b), (c)&(d) Cross-section SEM images of the fretting wear scar produced on duplex chameleon/PEO coating under 20 N load against a steel ball in air after 10^4 fretting cycles under 100 μm displacement amplitude.

Figure 21. Schematic illustration of the fretting wear process (a) and the surface stress distribution (b).

Figure 22. Cross-section SEM images of the fretting wear scar produced on duplex chameleon/PEO coating under 15 N load against steel ball in air after 10^4 fretting cycles under 100 μm displacement amplitude.

Table 1. Hardness and Young's modulus of as-deposited PEO and duplex coatings.

PEO coating		Duplex chameleon/PEO coating	
Hardness (GPa)	Young's modulus (GPa)	Hardness (GPa)	Young's modulus (GPa)
13.6 ± 7.2	185.0 ± 53.5	1.2 ± 0.6	29.1 ± 15.4

Table 2. Volume losses of wear scars obtained on duplex chameleon/PEO coatings under different test conditions, as derived from laser confocal topography maps.

Volume loss ($x10^{-4}$ mm^3)	Test conditions		
	In dry N_2 (20 N)	In air	
		20 N	15 N
Against alumina ball	1.41 ± 0.18	4.98 ± 0.09	—
Against steel ball	13.94 ± 0.08	7.92 ± 0.40	4.73 ± 0.06

Table 3. MoS_2 E^1_{2g}/A_{1g} peak ratios reflecting degree of MoS_2 crystallization and in plane graphite crystallite sizes from the Raman spectra presented in Fig.15

	Test conditions (Counterpart/Environment/20 N)				
	As-deposited chameleon	Steel ball		Alumina ball	
		N_2	Air	N_2	Air
Ratio of (E^1_{2g}/A_{1g}) peaks reflecting crystallization of MoS_2	0.92	0.96	0.95	0.94	0.88
In-plane graphite crystallite size L_a(nm)	15.15	14.68	17.61	16.04	17.57

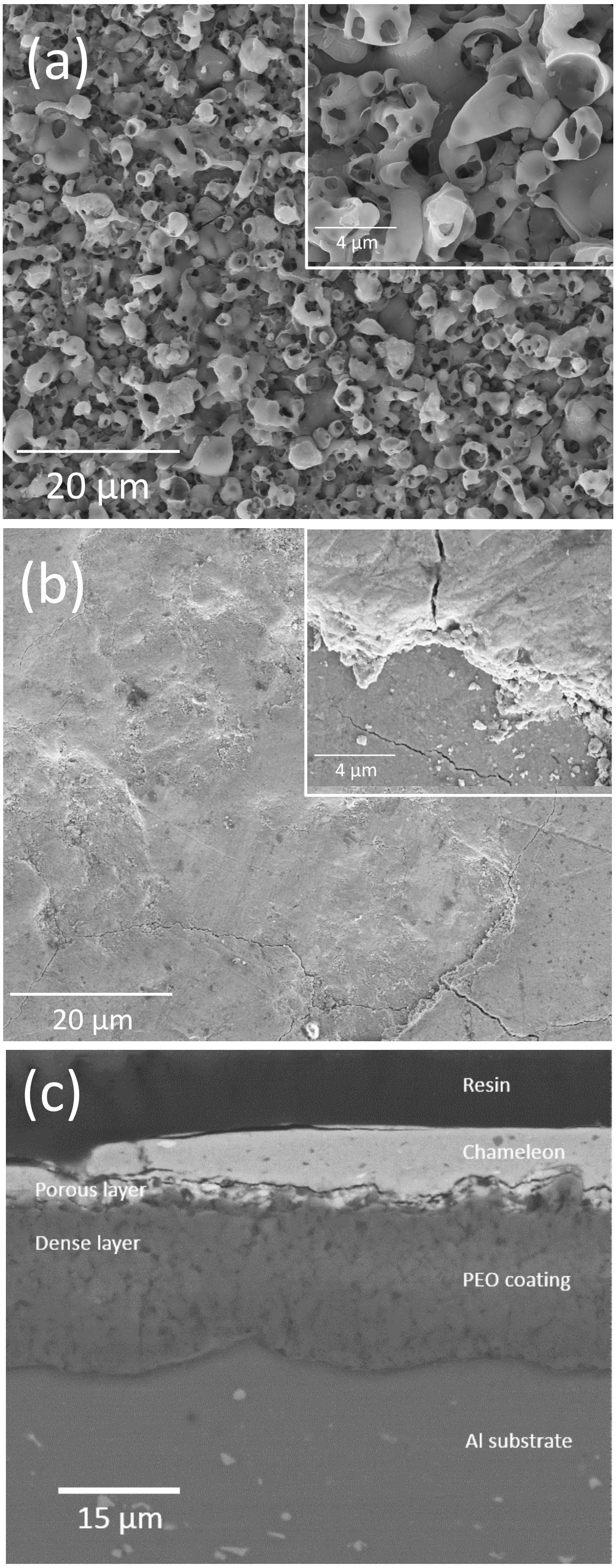

Figure 1. Surface morphologies of PEO coating (a), duplex chameleon/PEO coating (b) and cross-sectional morphology of the duplex chameleon/PEO coating (c) studied in this work.

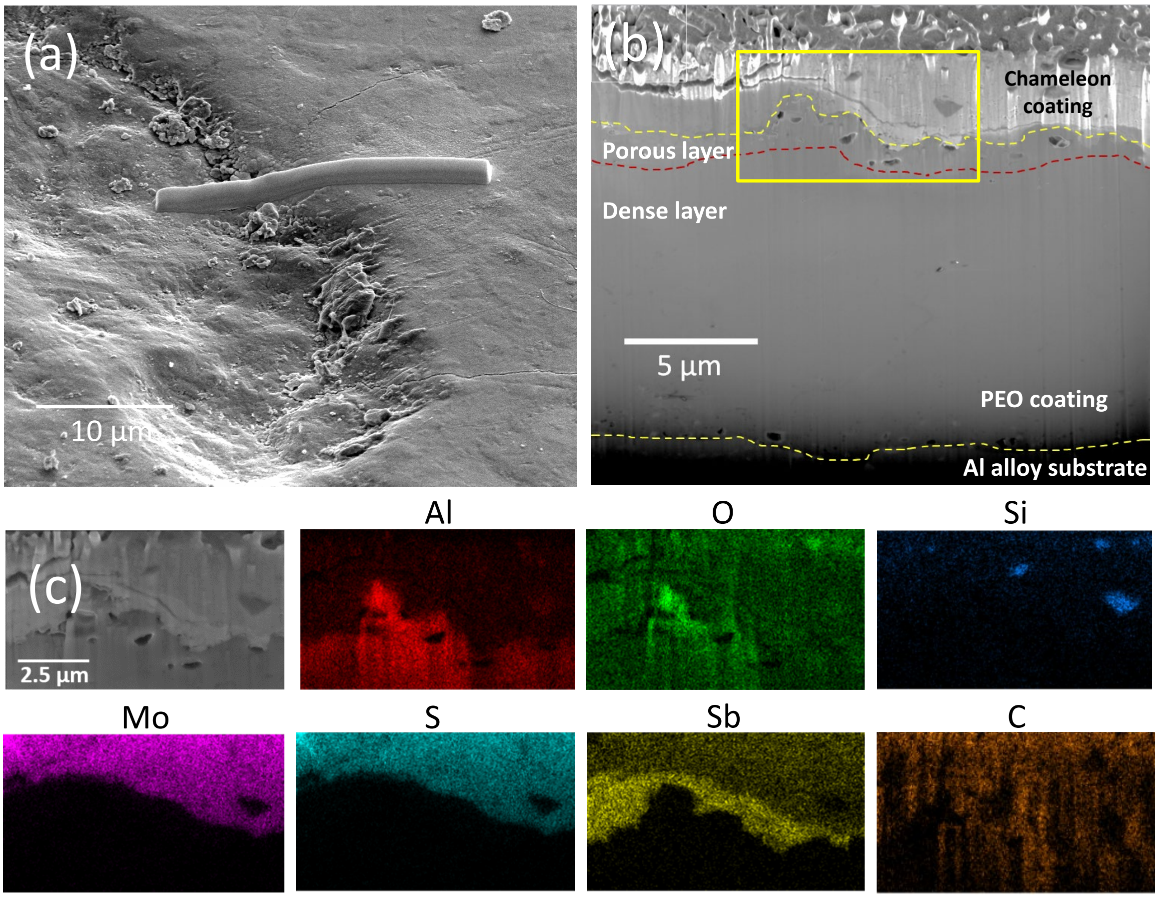

Figure 2. Cross-section of as-deposited duplex chameleon/PEO coating prepared by FIB milling technique: (a) location of the FIB milling on the coating surface observed as the stage tilt 30°; (b) coating cross section image; and (c) chameleon/PEO interfacial cross-section with elemental distribution maps.

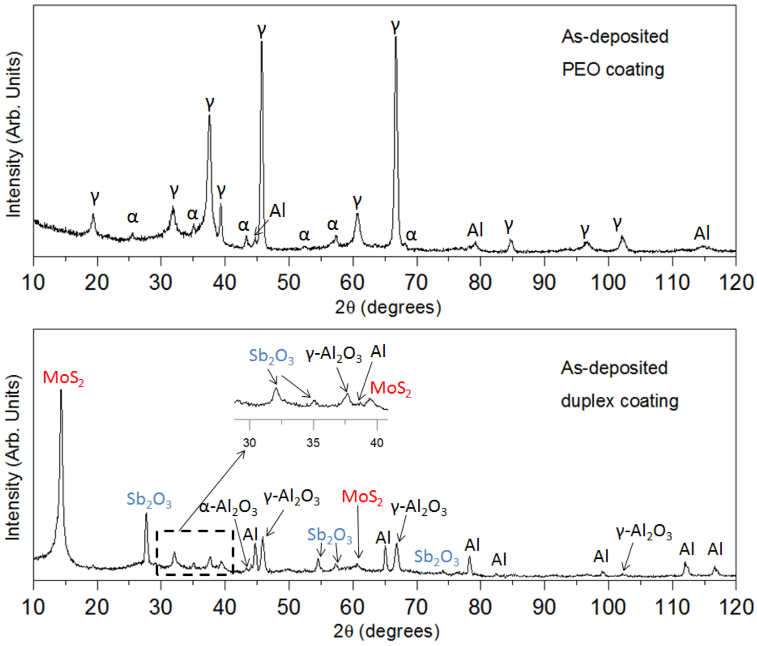

Figure 3. X-ray diffraction patterns of as-deposited PEO and duplex chameleon/PEO coatings.

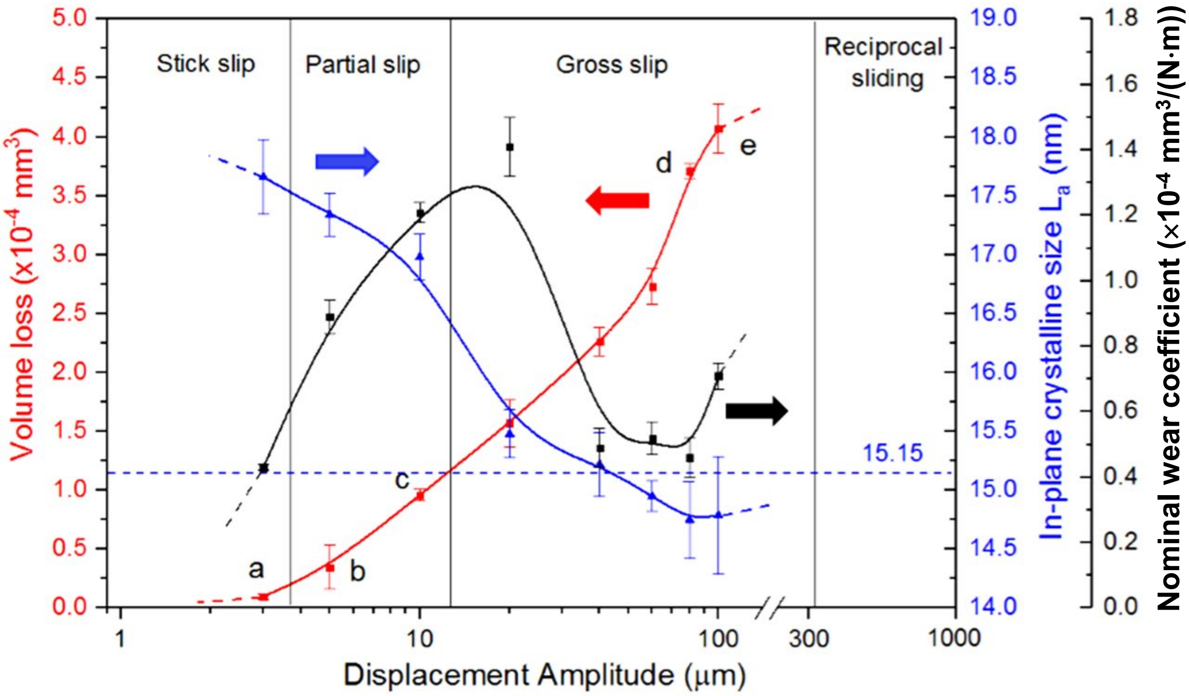

Figure 4. Fretting map of duplex chameleon-PEO coating on Al against steel counterpart in humid air showing dependencies of the volume loss, nominal wear coefficient and calculated in-plane crystalline size L_a of graphite phase in chameleon layer on displacement amplitude. The optical images of the five typical wear scars (a-e) are shown in Figure 6.

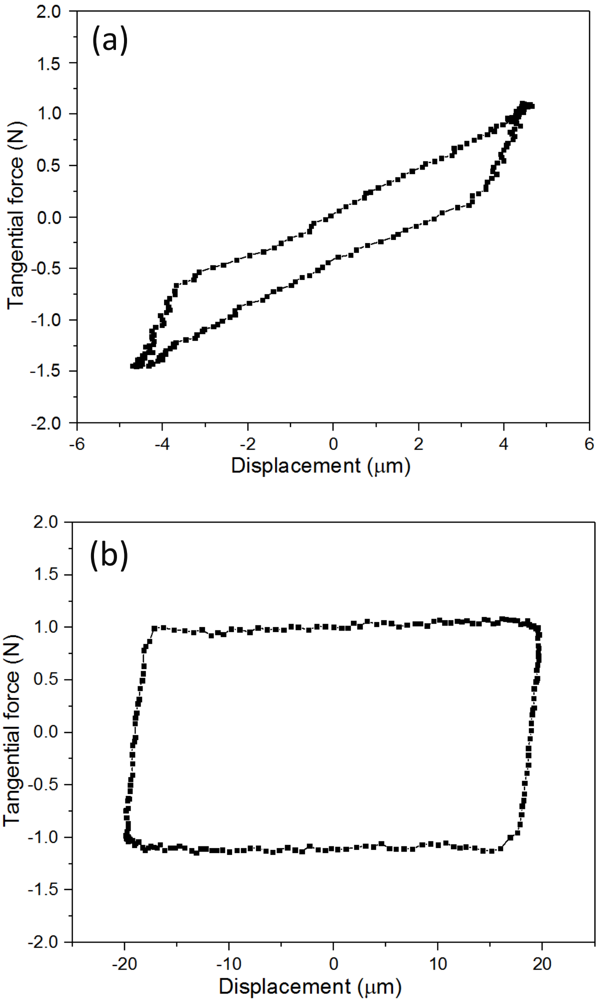

Figure 5. Typical examples of fretting loops for duplex chameleon-PEO coatings against steel in humid air in the partial (a) and gross (b) slip regimes.

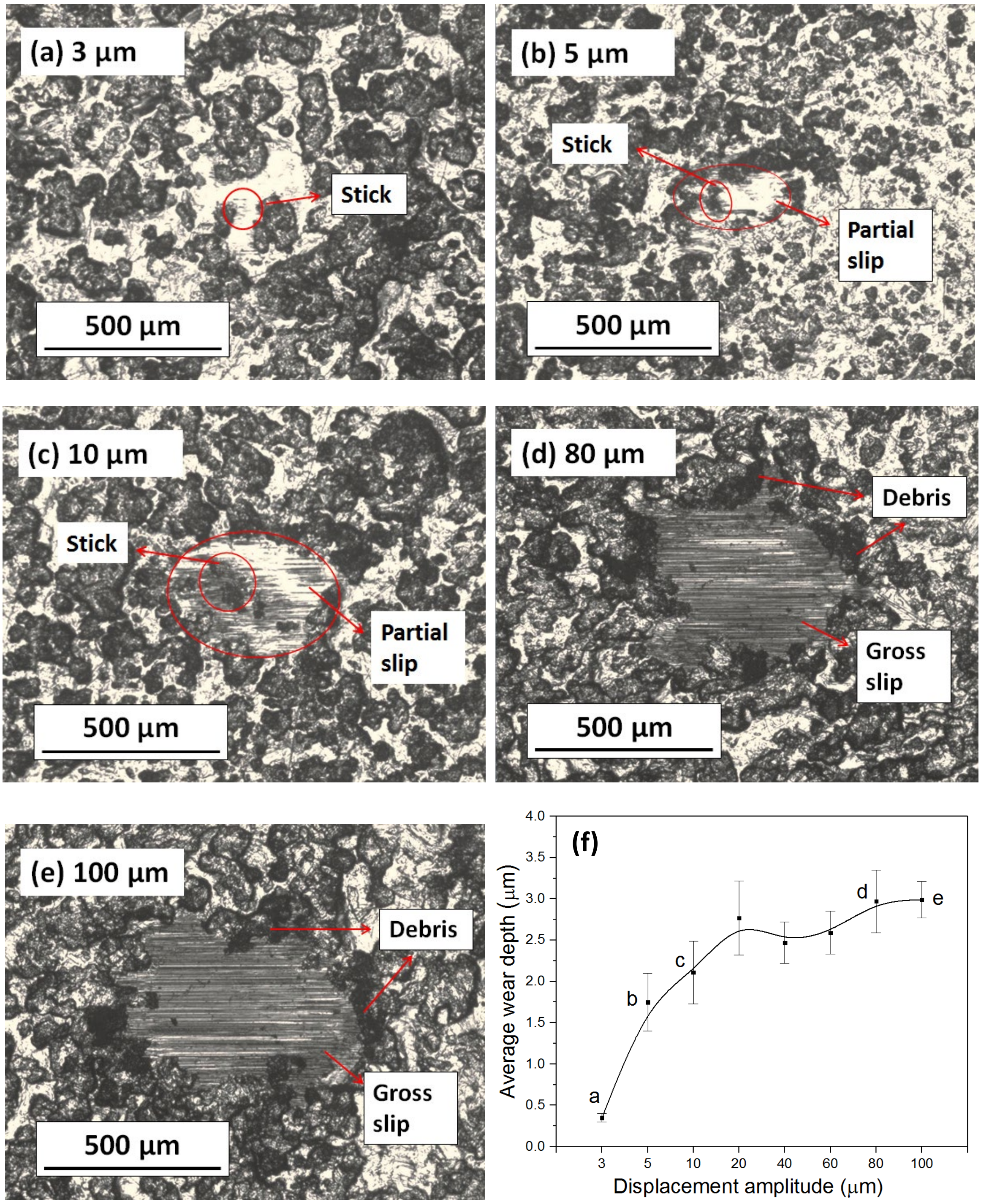

Figure 6. Optical micrographs of scars obtained in fretting wear tests of different amplitudes (a-e) and corresponding average wear depths (f).

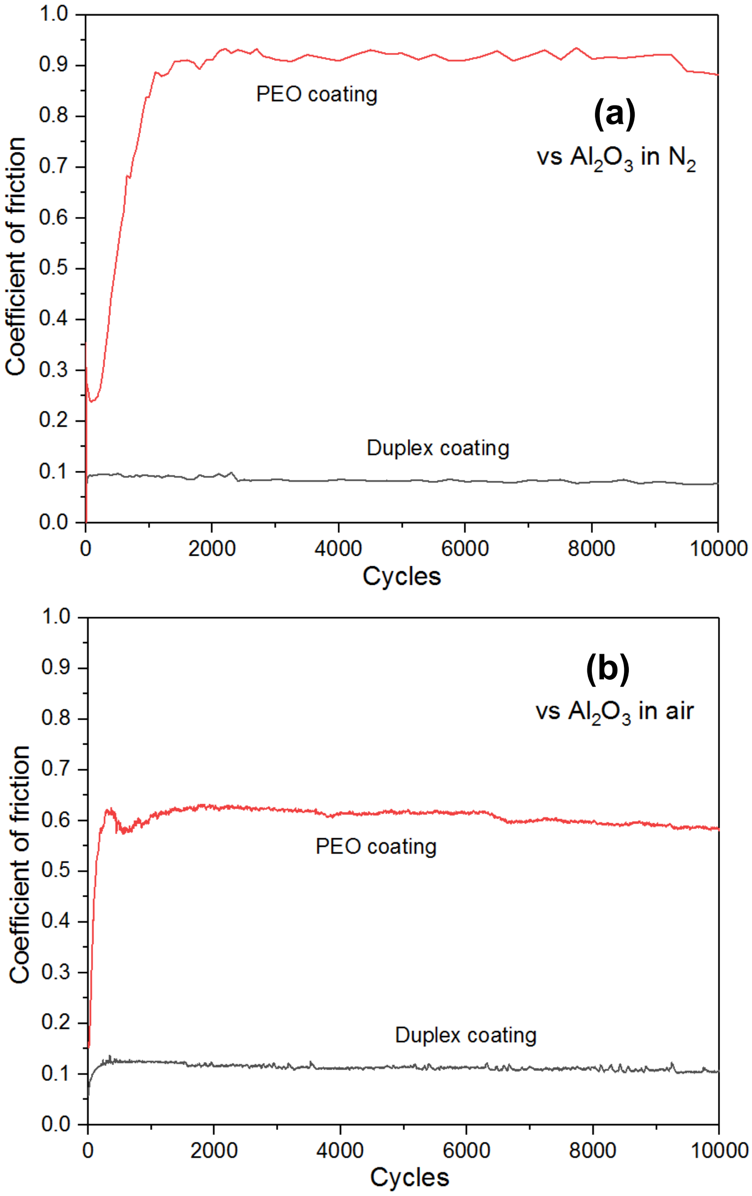

Figure 7. Evolution of coefficient of friction for PEO and duplex chameleon/PEO coatings under 20 N against alumina balls in N_2 (a) and air (b) (adapted from [27]).

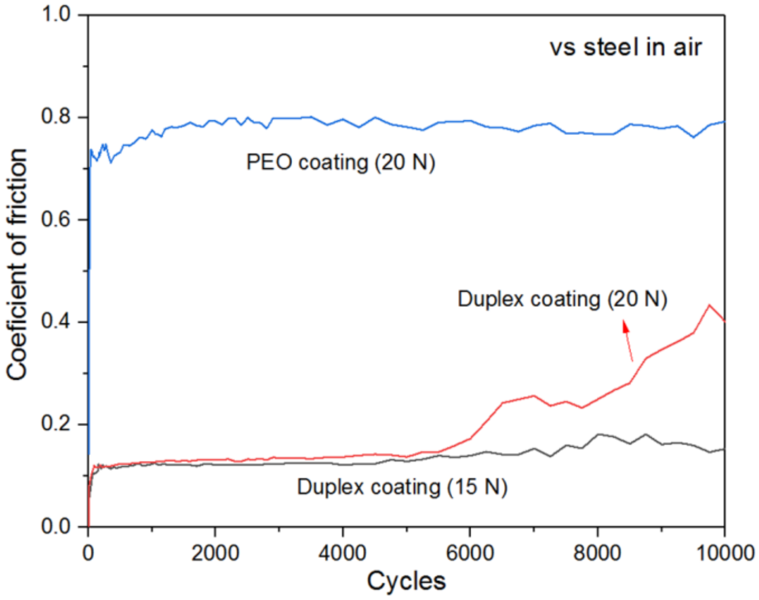

Figure 8. Evolution of coefficient of friction for PEO and duplex chameleon/PEO coatings under 15 N/20 N against steel balls in air.

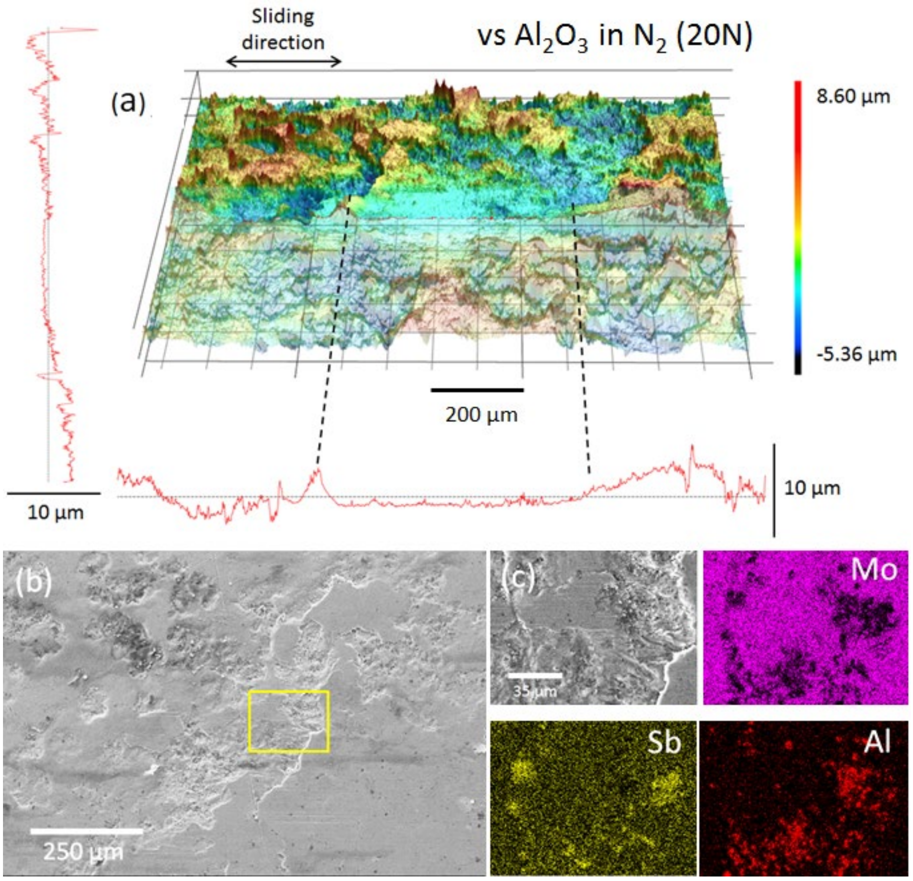

Figure 9. Laser confocal topography (a) and SEM/EDS images (b) & (c) of the wear scar produced under 20 N load against an alumina ball in N_2 after 10^4 fretting cycles under 100 µm displacement amplitude.

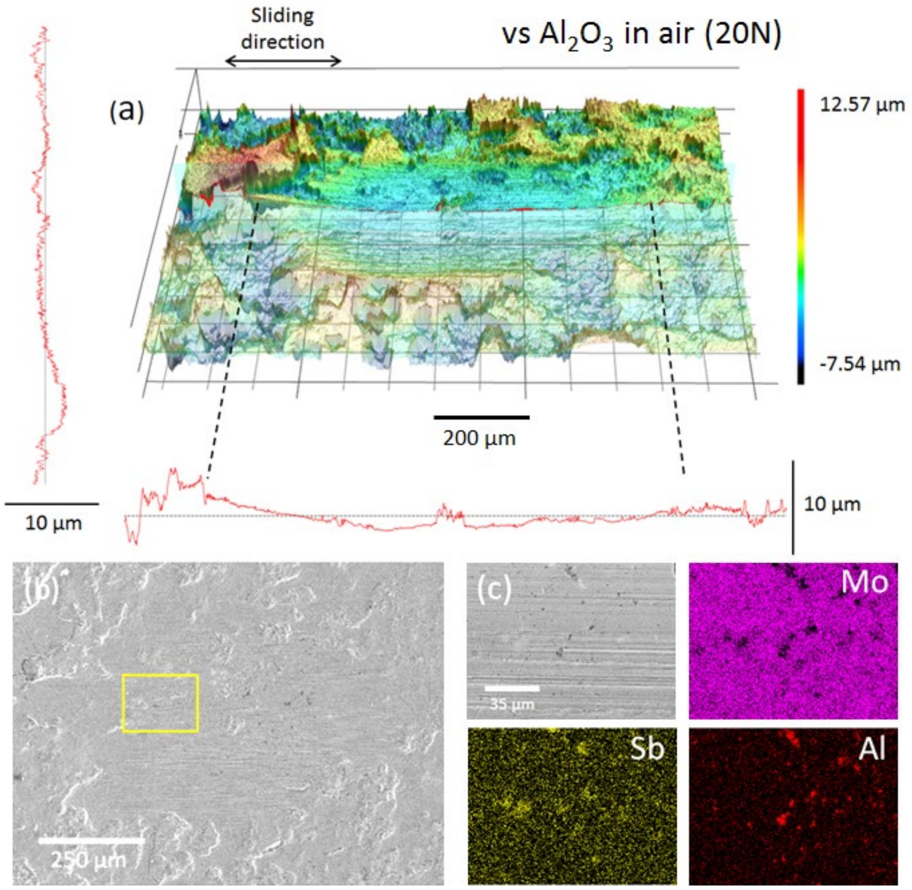

Figure 10. Laser confocal topography (a) and SEM/EDS images (b) & (c) of the wear scar produced under 20 N load against an alumina ball in air after 10^4 fretting cycles under 100 μm displacement amplitude.

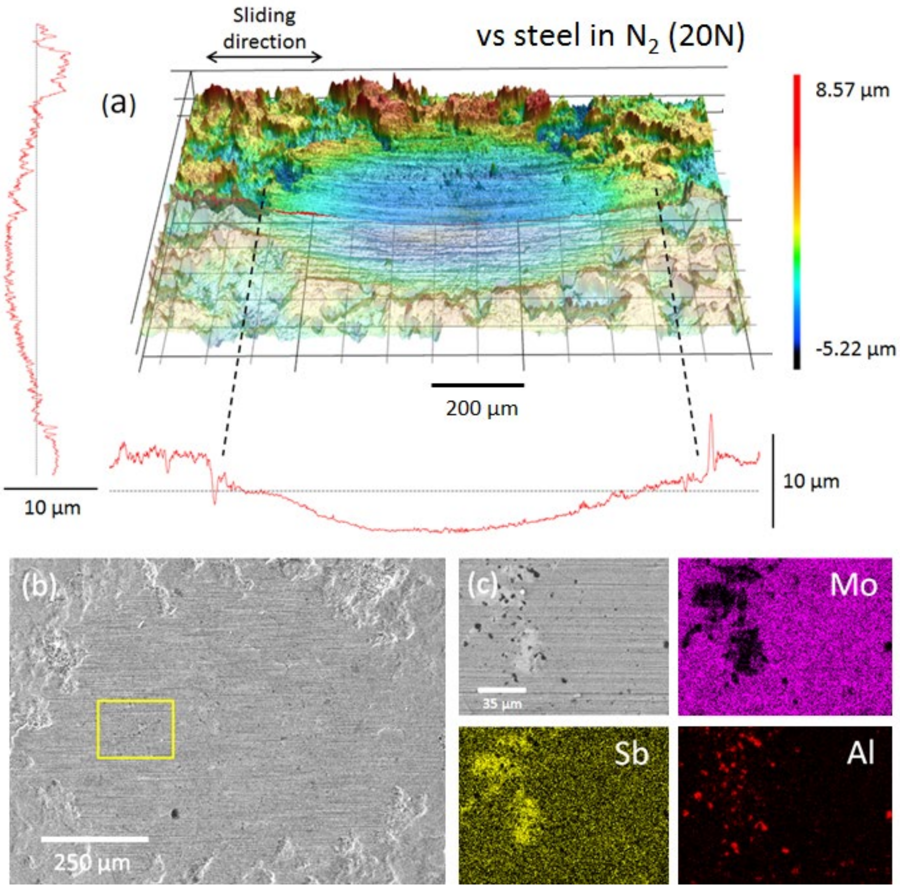

Figure 11. Laser confocal topography (a) and SEM/EDS images (b) & (c) of the wear scar produced under 20 N load against a steel ball in N_2 after 10^4 fretting cycles under 100 µm displacement amplitude.

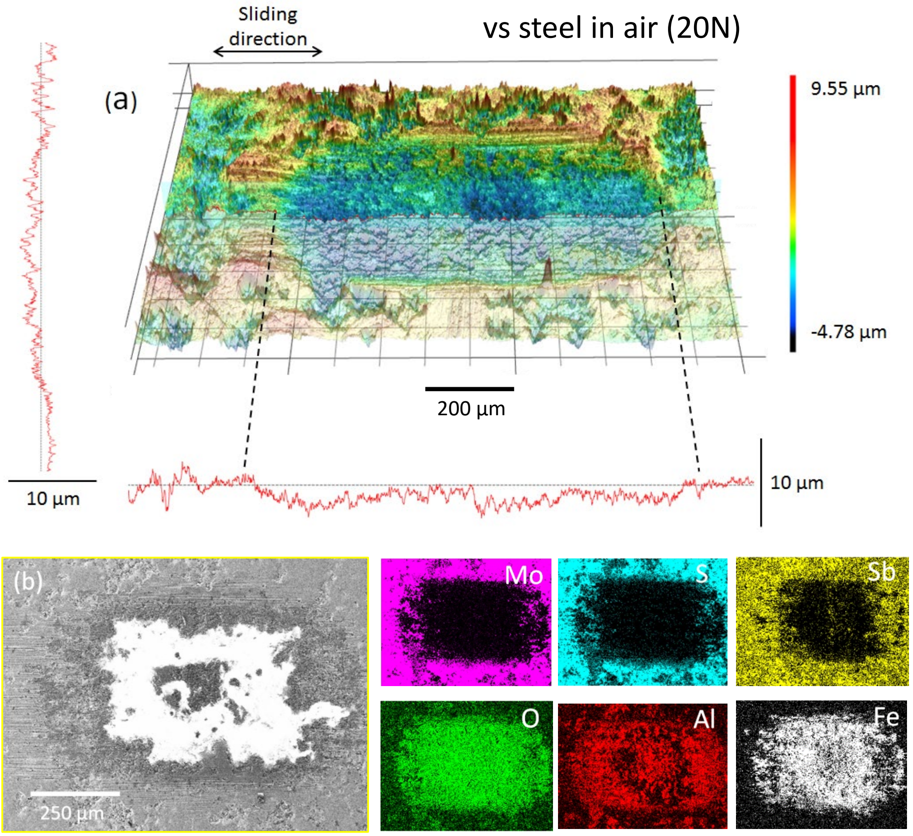

Figure 12. Laser confocal topography (a) and SEM/EDS images (b) & (c) of the wear scar produced under 20 N load against a steel ball in air after 10^4 fretting cycles under 100 μm displacement amplitude.

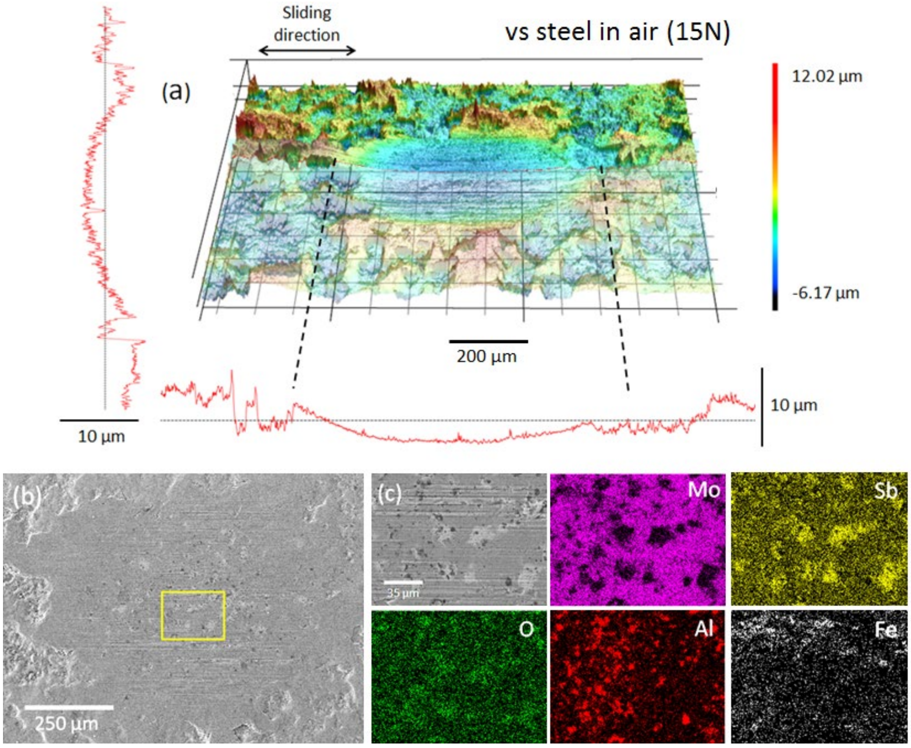

Figure 13. Laser confocal observation (a) and SEM/EDS images (b) & (c) of the wear scar tested under 15 N load against steel ball in air after 10^4 fretting cycles under 100 μm displacement amplitude.

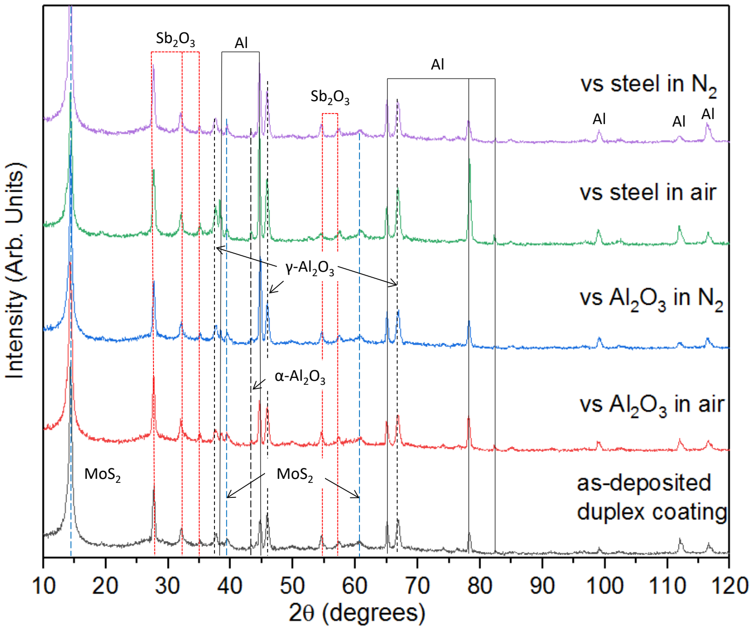

Figure 14. X-ray diffraction patterns obtained from within gross-slip fretting wear scars produced under 20 N loads, and of as-deposited duplex chameleon/PEO coating.

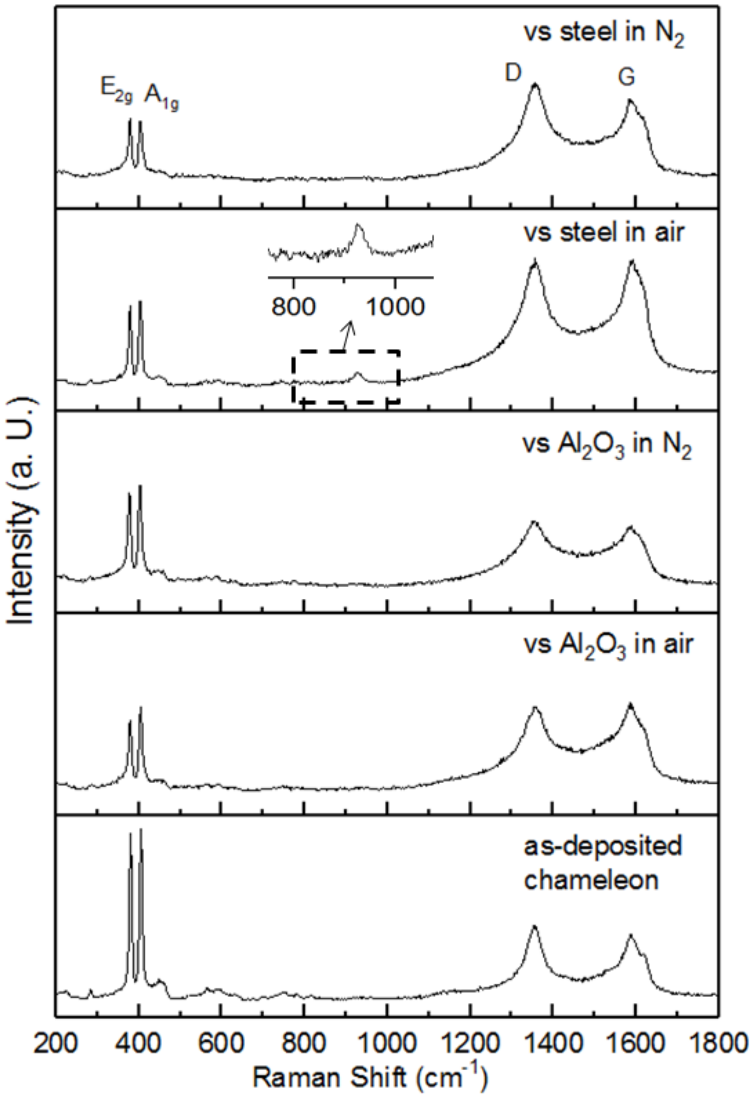

Figure 15. Raman spectra of the wear scars produced under 20 N loads and of as-deposited duplex chameleon/PEO coating.

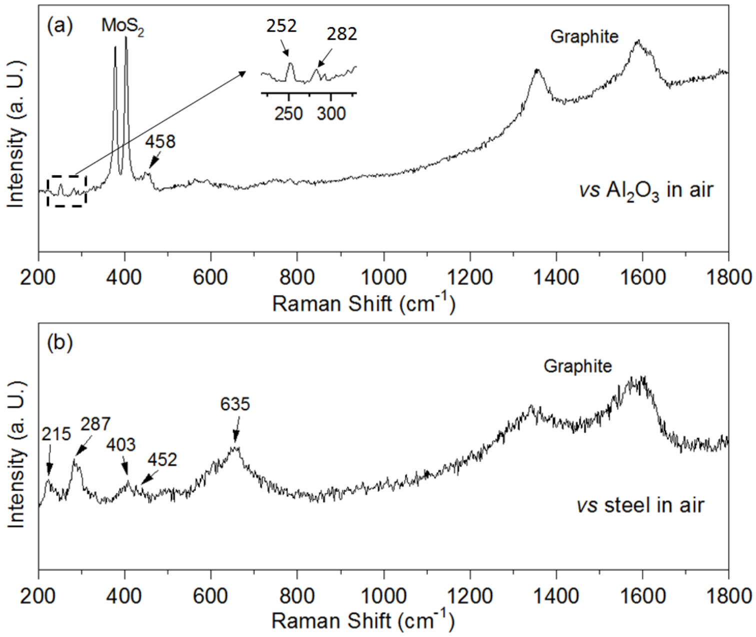

Figure 16. Raman spectra of the accumulated debris in the scars produced in air under 20 N loads, (a) against steel ball; (b) against alumina ball for fretting wear of duplex chameleon/PEO coating.

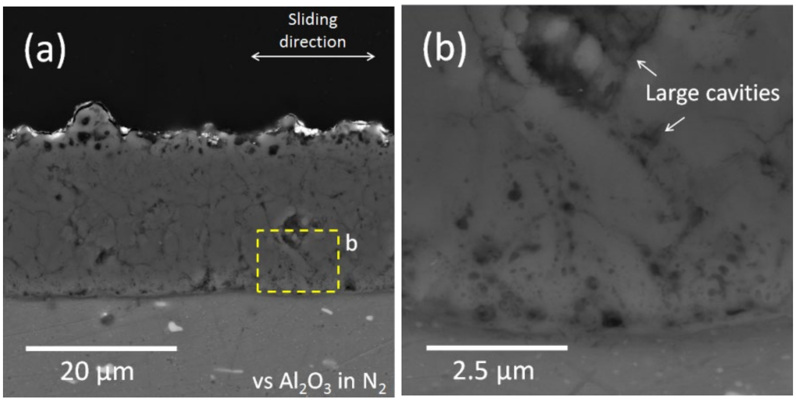

Figure 17. (a), (b) Cross-section SEM images of the fretting wear scar produced on duplex chameleon/PEO coating under 20 N load against alumina ball in N_2 after 10^4 fretting cycles under 100 µm sliding displacement amplitude.

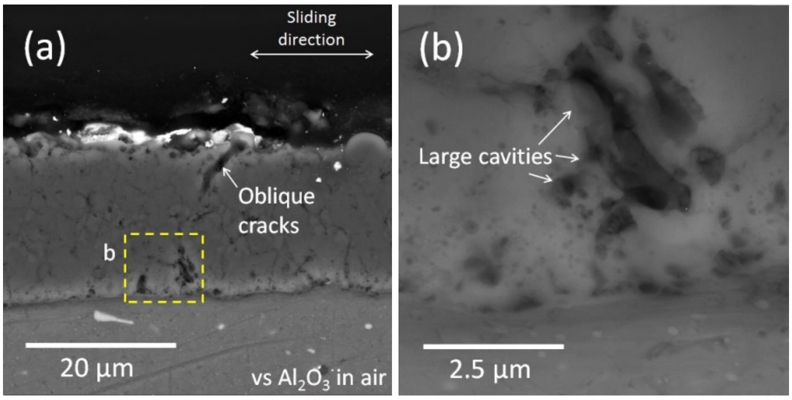

Figure 18. (a), (b) Cross-section SEM images of the fretting wear scar produced on duplex chameleon/PEO coating under 20 N load against alumina ball in air after 10^4 fretting cycles under 100 μm displacement amplitude.

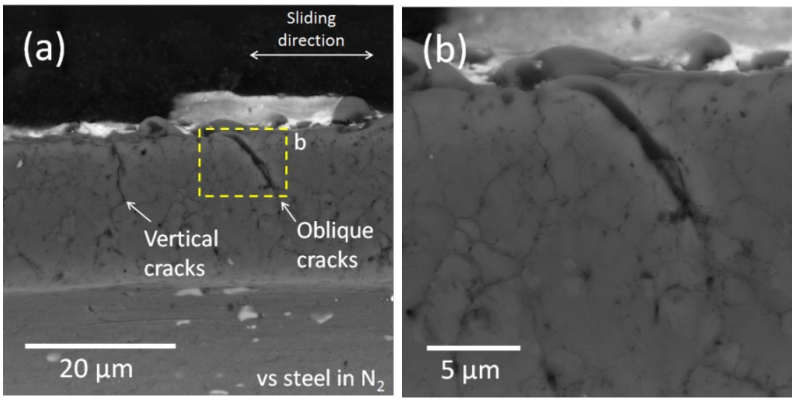

Figure 19. (a), (b) Cross-section SEM images of the fretting wear scar produced on duplex chameleon/PEO coating wear scar produced under 20 N load against steel ball in N_2 after 10^4 fretting cycles under 100 μm displacement amplitude.

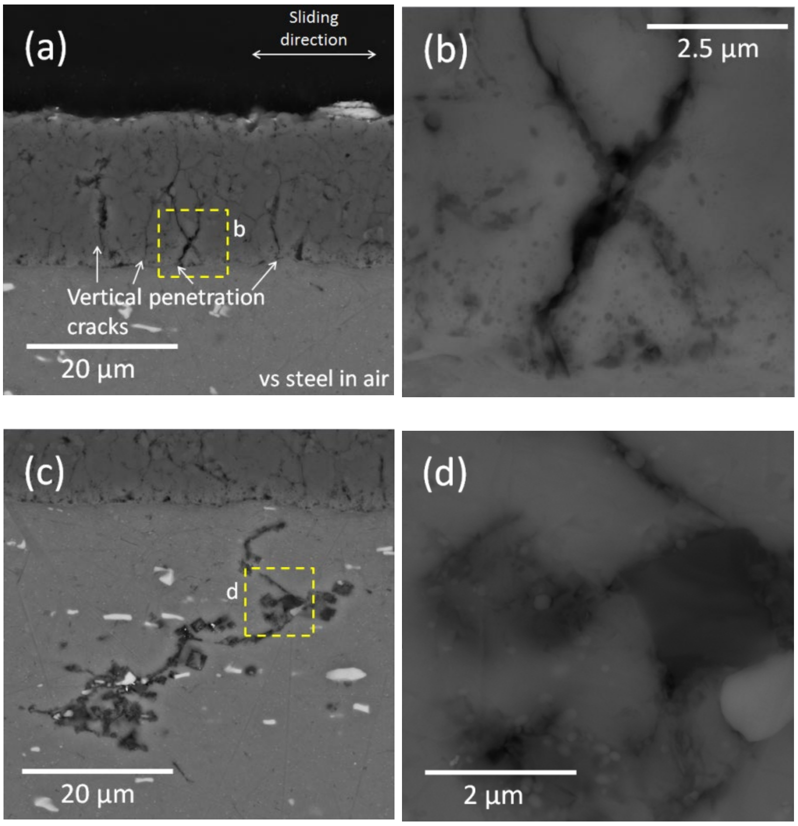

Figure 20. (a), (b), (c) and (d) Cross-section SEM images of the fretting wear scar produced on duplex chameleon/PEO coating under 20 N load against a steel ball in air after 10^4 fretting cycles under 100 µm displacement amplitude.

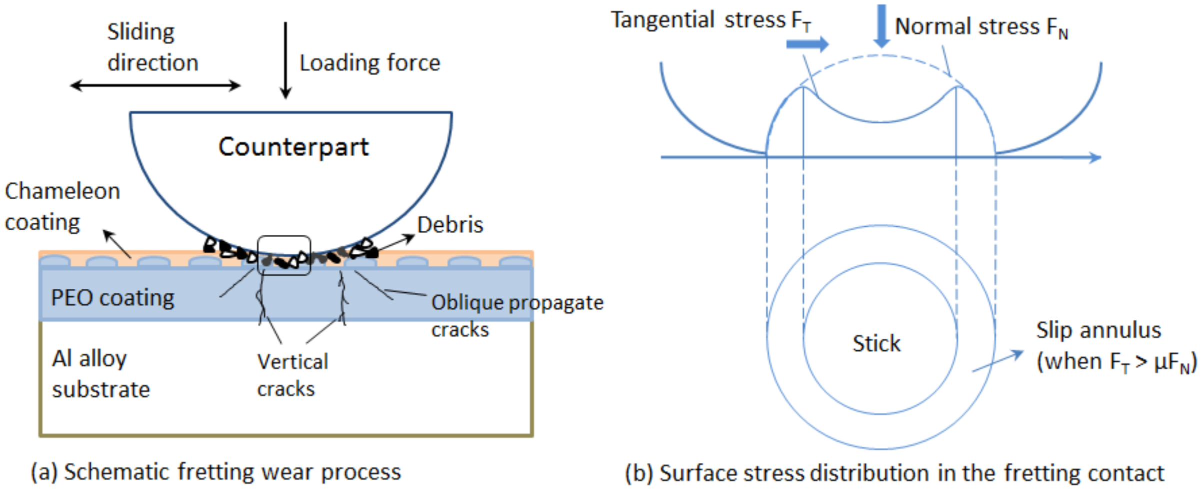

(a) Schematic fretting wear process

(b) Surface stress distribution in the fretting contact

Figure 21. Schematic illustration of the fretting wear process (a) and the surface stress distribution (b).

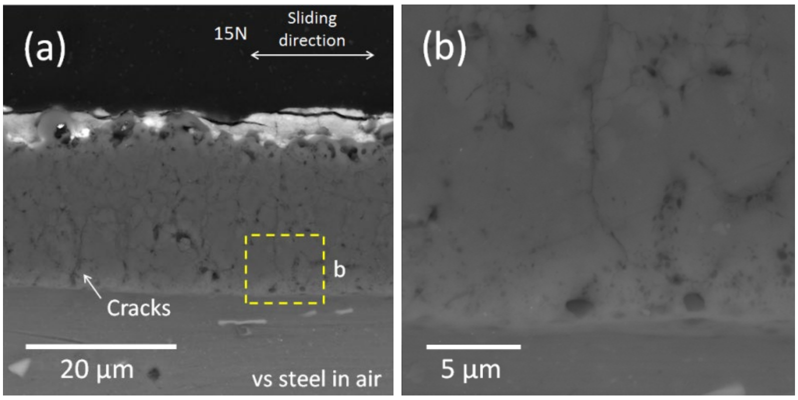

Figure 22. Cross-section SEM images of the fretting wear scar produced on duplex chameleon/PEO coating under 15 N load against steel ball in air after 10^4 fretting cycles under 100 μm displacement amplitude.